RMetS

Royal Meteorological Society

Using *in situ* estimates of ice water content, volume extinction coefficient, and the total solar optical depth obtained during the tropical ACTIVE campaign to test an ensemble model of cirrus ice crystals[†][‡]

Anthony J. Baran,[a]* Paul J. Connolly,[b] A. J. Heymsfield[c] and A. Bansemer[c]

[a]*Met Office, Exeter, UK*
[b]*School of Earth, Atmospheric and Environmental Sciences, University of Manchester, UK*
[c]*National Center for Atmospheric Research, Boulder, Colorado, USA*

*Correspondence to: A. J. BaranMet Office, Fitzroy Road, Exeter EX1 3PB, UK. E-mail: anthony.baran@metoffice.gov.uk
[†]The contribution of A. J. Baran was written in the course of his employment at the Met Office, UK and is published with the permission of the Controller of HMSO and the Queen's Printer for Scotland.
[‡]The contributions of A. J. Heymsfield and A. Bensemer were prepared as part of their official duties as US Federal Government employees.

An ensemble model of cirrus ice crystals combined with a parametrized particle size distribution function (PSD) is used to predict the ice water content (IWC), column-integrated IWC (ice water path, IWP), volume extinction coefficient, and the total solar optical depth, for five tropical cirrus cases. The PSD is estimated from the IWC and in-cloud temperature, and comparisons are presented between the ensemble model predictions and *in situ* estimates of these microphysical and macrophysical quantities. The *in situ* estimates were obtained during the Aerosol and Chemical Transport In tropical conVection (ACTIVE) campaign between November–December 2005 and January–February 2006, based at Darwin, Australia. The microphysical instrumentation deployed on the Airborne Australia Egrett research aircraft were the SPEC Cloud Particle Imaging (CPI) probe, Cloud and Aerosol Spectrometer (CAS) and Cloud Imaging Probe (CIP). The CPI was used to measure ice crystal size from about 5 to $1800\ \mu$m, ice crystal number concentration, and to estimate ice crystal shape, IWC, IWP, volume extinction coefficient and the total solar optical depth. The CIP instrument was also used to measure ice crystal size from about 25 to $1550\ \mu$m, ice crystal number concentration and to estimate IWC. For all flights the limited CPI shape recognition algorithm recorded that about 80% or greater of the ice crystal populations were composed of small irregular or 'quasi-spherical' ice crystals. The CPI- and CIP-estimated IWC distributions are compared against each other and it is shown that the distributions are not significantly different at the 95% level of confidence. The CPI-estimated averaged IWC ranged between approximately 5.3 and 98.2 mg m^{-3}. The CPI-estimated IWP and total solar optical depth ranged between $\sim 1.0 \pm 0.5$ and 35.0 ± 17 g m^{-2} and between 0.1 ± 0.05 and 1.46 ± 0.73, respectively.

To predict the IWC and IWP, an ensemble model effective density-size relationship is derived, and it is shown that the uncertainty in the model predictions are generally within the uncertainty of the CPI estimates for all cases considered. It is also demonstrated that, when the CPI-estimated total solar optical depth is greater than unity, the ensemble model combined with the PSD scheme predicts an uncertainty in the volume extinction coefficient and total solar optical depth that is within the CPI experimental range of uncertainty. However, for total solar optical depths much less than unity, the ensemble model combined with the PSD scheme does not generally predict an uncertainty in the volume extinction coefficient and total solar optical depth that is within the lower range of the CPI uncertainty; the physical reason for this is further explored.

The paper demonstrates that there is predictive value in combining an ensemble model of ice crystals with a universal PSD scheme to predict the microphysical and macrophysical properties of importance to radiative transfer through tropical cirrus. Moreover, in the case of very low IWC tropical cirrus, further characterization of the PSD is required using a number of *in situ* instruments. Copyright © Royal Meteorological Society and Crown Copyright, 2011

1.   Introduction

Cirrus can cover up to 30% of the midlatitudes at any one time, and in the Tropics this can increase to 60–70% (Liou, 1986; Wylie and Menzel, 1999; Sassen and Comstock, 2001; Stubenrauch *et al.*, 2006; Hong *et al.*, 2007; Sassen *et al.*, 2008). The satellite-based cirrus climatology shows that the cloud is not confined to a particular season or time, and that in the Tropics it can be ubiquitous (Hong *et al.*, 2007; Sassen *et al.*, 2008). With such a spatial and temporal distribution, cirrus is an important cloud type for the Earth–atmosphere radiation balance (Liou, 1986; Stephens *et al.*, 1990; Donner *et al.*, 1997; Kristjánsson *et al.*, 2000; Edwards *et al.*, 2007). In the most recent (fourth) assessment report of the Intergovernmental Panel on Climate Change (IPCC, 2007), it was concluded that the magnitude of the cloud feedback (the degree to which a cloud either amplifies or diminishes the surface warming of the Earth's surface under CO_2 forcing) represents one of the greatest uncertainties in current climate general circulation models (GCMs). In order to further constrain parametrizations of cirrus within GCMs so that the uncertainty in the magnitude of its feedback is reduced, it is necessary to measure on a global scale the hydrological and radiative properties of these clouds. Such a comprehensive set of space-based measurements of cirrus that can be utilized over a wide range of wavelength and/or frequency space to assess GCM representations of cirrus have only become available more recently (e.g. Waliser *et al.*, 2009).

The magnitude of the cloud feedback not only depends on the spatial and temporal distribution of the cloud but also on its microphysical and macrophysical composition. In the case of cirrus, determining the magnitude of its feedback is particularly problematic since this cloud is composed of non-spherical ice crystals of varying shapes and sizes as well as varying ice water content (IWC), and these properties may well vary considerably from cloud top to cloud bottom (e.g. reviews by Liou, 1986; Lynch *et al.*, 2002; Baran, 2009; and references contained therein). Theoretical calculations by Zhang *et al.* (1999) demonstrated that it is possible to change the sign of the cirrus feedback from negative (cooling, due to reflection of incident sunlight) to positive (warming, due to absorption of upwelling terrestrial radiation) by changing the microphysical composition of the cloud whilst keeping the macrophysical properties of the cloud constant. It was shown that, for mean ice crystal sizes of less than about 50 μm, it was possible to produce a net cooling of about -40 W m^{-2}. In contrast, for mean ice crystal sizes greater than about 150 μm, it was possible to produce a net warming of about 20 W m^{-2}. More recently, theoretical calculations by Fu (2007) have shown that, on changing the aspect ratio (the ratio of length to diameter) of ice crystals from unity to 0.1, the net short wave forcing could change from -30 to -70 W m^{-2}. These calculations were based on the assumptions of the cirrus optical depth (the integral product of the cloud vertical geometric thickness and volume extinction coefficient) being set to 4, and completely overcast skies.

Recent work by Choi and Hoi (2006) used space-based measurements located over the Tropics (25°N–25°S) to estimate the optical depth required to change the cirrus feedback from net warming to net cooling. They found that, for optical depths less than 10, or for optical depths equal to or greater than 10, cirrus was determined to be net warming

or net cooling, respectively. For optical depths less than 9, they found that cirrus can significantly influence the energy balance of the Tropics. Given that the climatology of cirrus in the Tropics can reach approximately 70%, determining the magnitude of this warming is of particular importance since these clouds exert a major influence on the energy balance of the Tropics.

Determining the magnitude of the net warming of optically thin tropical cirrus is problematic since, as previously discussed, these clouds consist of a variety of ice crystal shapes and sizes as well as a large range in IWC. To add to this complexity, more recent observations of tropical cirrus have revealed that fresh anvils can consist of hexagonal ice plates and complex arrays of compact and spatial plate-like aggregates as well as more indeterminate ice crystal shapes (Stith *et al.*, 2000; Lawson *et al.*, 2003; Connolly *et al.*, 2005; Um and McFarquhar, 2009). Um and McFarquhar (2009) showed that plate-like aggregates on some occasions could dominate the bulk extinction of the cloud. In contrast to fresh anvils, more mature tropical cirrus outflows are mostly composed of bullet-rosettes and polycrystals, as well as indeterminate irregular non-symmetric ice crystals which are probably composed of planar crystals (McFarquhar and Heymsfield, 1996; Lynch *et al.*, 2002; Whiteway *et al.*, 2004; Lawson *et al.*, 2008). However, these more indeterminate asymmetric ice crystals may contain elements which are symmetric, as demonstrated by Stoelinga *et al.* (2007). Also, hexagonal ice plates of aspect ratio 6:1 with sizes of up to 100 μm have been observed near the tropical tropopause by Jensen *et al.* (2008), and these ice crystals were not associated with deep tropical convection.

Predicting the optical properties of such an ensemble of observed ice crystal shapes and sizes that exist in tropical cirrus is difficult, and the review of Baran (2009) describes the light-scattering methods and approaches that are currently being applied to this problem. However, it is worth pointing out here that, given the range of space-based measurements in wavelength or frequency space now available (Waliser *et al.*, 2009), it is important to base GCM predictions of the sign and size of the cirrus feedback on optical properties that can be consistently applied across the electromagnetic spectrum. Single ice crystal models such as the pristine hexagonal ice column cannot be consistently applied across the long wave and short wave regions of the spectrum, as demonstrated by Baran *et al.* (2003) and Baran and Francis (2004). Research carried out by a number of authors (Francis *et al.*, 1999; Rolland *et al.*, 2000; Liou *et al.*, 2000; Baran *et al.*, 2001; McFarquhar *et al.*, 2002; Jourdan *et al.*, 2003; Baum *et al.*, 2005, 2007; Baran and Labonnote, 2007; Baran *et al.*, 2009) suggests that the radiative properties of cirrus are better represented by an ensemble model of cirrus ice crystals rather than single ice crystal models. Indeed, single ice crystal models have been shown to poorly represent the measured radiometric as well as the observed bulk macrophysical and microphysical properties of cirrus (Francis *et al.*, 1999; Liou *et al.*, 2000; Baran *et al.*, 2001; Baum *et al.*, 2005). Baum *et al.* (2005) constructed an ensemble ice crystal model that attempts to replicate *in situ* measurements of the ice crystal shape distribution by constructing geometrical idealizations of the observed shape distribution. The ensemble of ice crystals adopted by Baum *et al.* (2005) incorporates droxtals to take account of small ice crystals less than 100 μm in size; Yang *et al.* (2003) give further details. For sizes greater than 100 μm, the ensemble consists of hexagonal

ice columns and plates, hollow columns, bullet-rosettes and hexagonal ice aggregates. It was demonstrated by Baum *et al.* (2005) that this ensemble could replicate the measured IWC and the median mass diameter of measured particel size distributions (PSDs) collected during a number of field campaigns located in the midlatitudes and Tropics. The single-scattering properties predicted by the ensemble model of Baum *et al.* (2005) currently form the basis of the space-based MODerate resolution Imaging Spectroradiometer (MODIS; Platnick *et al.*, 2003) retrievals of cirrus macrophysical and microphysical properties (Hong *et al.*, 2007). However, the single-scattering properties predicted by the Baum *et al.* (2005) model retain the hexagonal symmetries of the individual ice crystals that are used to construct the shape distribution. This means that the 22° and 46° halo features as well as backscattering features are still retained in the scattering patterns of the ensemble model used for MODIS retrievals of cirrus microphysical and macrophysical properties.

Given the variability of ice crystal shapes and sizes that exist in cirrus, the paper by Baran and Labonnote (2007) posed the question as to whether the bulk macrophysical and radiative properties of cirrus could be predicted by some generalized ensemble of ice crystals that was combined with a generalized PSD. In that paper, a self-consistent scattering model of cirrus is introduced in which it is shown that, when an ensemble model of cirrus ice crystals is combined with a PSD scheme, the ice mass is conserved and the bulk extinction of the cloud can be predicted to generally within a factor two of *in situ* measurements obtained in the midlatitudes and Tropics.

Moreover, it is also demonstrated in Baran and Labonnote (2007) that, by randomising each ice crystal member of the ensemble, which removed the 22° and 46° haloes from the predicted scattered intensity of the ensemble model, then global space-based measurements of the total reflection properties of cirrus between the scattering angles of about 60° to 180° could be replicated. The details of the ensemble model have been previously described in Baran and Labonnote (2007) but a brief description is given here. The ensemble model consists of six idealized geometrical models, shown in Figure 1. The first of these is the hexagonal ice column assuming an aspect ratio of unity, the second is the six-branched bullet-rosette, and thereafter hexagonal elements are arbitrarily attached as a function of ice crystal maximum dimension, which is supposed to represent the process of ice crystal aggregation. By arbitrarily attaching hexagonal elements, the ensemble model becomes progressively more complex and spatial with the third ice crystal consisting of a three-branched hexagonal aggregate, then a five-branched hexagonal aggregate, eight-branched hexagonal aggregate and finally a ten-branched hexagonal chain-like aggregate is constructed. These six ice crystals are distributed sequentially across the PSD with the single hexagonal column representing the smallest ice crystal maximum dimensions and the ten-branched hexagonal aggregate representing the largest ice crystal maximum dimensions. The other four ice crystals are distributed sequentially within the PSD between the hexagonal column and ten-branched hexagonal aggregate.

The PSD scheme used in Baran and Labonnote (2007) has been previously described in Field *et al.* (2007). The PSD scheme consists of a parametrization of many *in situ* measured PSDs obtained in the midlatitudes and Tropics. It
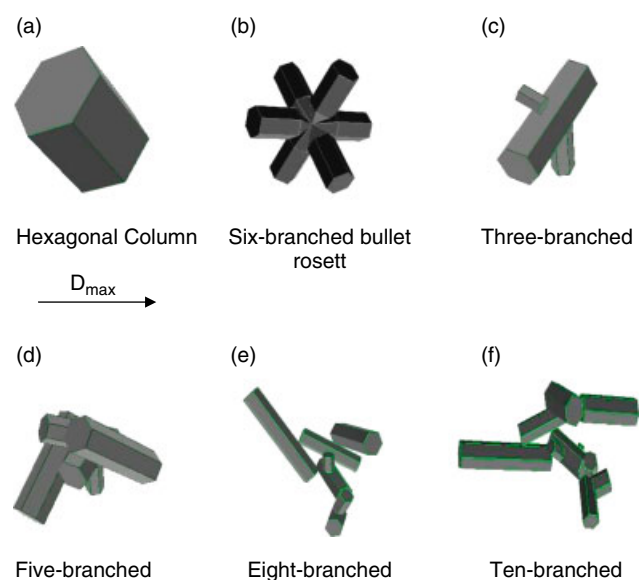

Figure 1. The ensemble model of cirrus ice crystals in order of increasing maximum dimension (D_{max}): (a) hexagonal ice column of aspect ratio unity, (b) six-branched bullet-rosette, (c) three-branched aggregate, (d) five-branched aggregate, (e) eight-branched aggregate and (f) ten-branched aggregate This figure is available in colour online at wileyonlinelibrary.com/journal/qj

is shown by Field *et al.* (2005, 2007) that the many *in situ* measured PSDs can be generalized into one universal PSD generated from the IWC and in-cloud temperature. The PSD parametrization developed in Field *et al.* (2007) is based on *in situ* measurements obtained between the temperatures of 0 and −60°C and includes the contribution of small ice crystals of less than 100 μm in size to the PSD. The inclusion of the small ice crystal contribution to the parametrized PSD was achieved in Field *et al.* (2007) by using the measured interarrival time of each ice crystal to filter out the ice crystal population that was due to shattering for sizes greater than 100 μm. For ice crystal sizes less than 100 μm, the PSD was extrapolated by assuming an exponential function. This filtering out of the shattered ice crystal population is important to perform due to the well-known problem of ice crystal shattering on the inlet of the *in situ* microphysical probes (Field *et al.*, 2006; Heymsfield, 2007; McFarquhar *et al.*, 2007). It should also be pointed out that, in the parametrization of the PSD due to Field *et al.* (2007), there is no information on ice crystal shape.

In the paper by Baran *et al.* (2009), the ensemble model of Baran and Labonnote (2007) and the PSD parametrization due to Field *et al.* (2007) are used to show that for several midlatitude cirrus cases the ensemble model can predict, to generally within the current experimental uncertainties of ±50%, the Cloud Particle Imaging (CPI)-estimated IWC, ice water path (IWP), volume extinction coefficient and the total solar optical depth. In the same paper, it is also shown that these quantities are of fundamental importance to the prediction of the bulk radiative properties of cirrus and can be predicted without recourse to the concept of an ice crystal effective dimension. In Baran *et al.* (2009), the Brown and Francis (1995) and Matrosov (1999) effective density–size relationships are applied to the ensemble model to best predict the CPI-estimated IWC and IWP. However, in this article the true mass of the model crystals are used assuming the density of solid hexagonal ice.

In this article the work of Baran and Labonnote (2007) and Baran *et al.* (2009) is extended by using *in situ* CPI estimates of tropical cirrus IWC, IWP, volume extinction coefficient, and the total solar optical depth to further test the predictive value of the *same* ensemble model combined with the PSD scheme for the case of tropical cirrus. It is important to demonstrate that any ice crystal model of cirrus has a predictive value that is not dependent on location. The paper is split into the following sections. Section 2 briefly describes the Aerosol and Chemical Transport In tropical conVection (ACTIVE) campaign, the *in situ* microphysical measurements, and the types of cirrus sampled. Section 3 defines the macrophysical and microphysical quantities to be predicted and the methodology of testing the ensemble model. Section 4 presents the results of comparing the ensemble model predictions of tropical IWC, IWP, volume extinction coefficient, and the total solar optical depth against the *in situ* CPI estimates of these quantities. Section 5 describes the findings of this article in the summary.

2. The ACTIVE campaign and *in situ* measurements

The details of the ACTIVE campaign have been previously described by Vaughan *et al.* (2008) and May *et al.* (2009). However, a brief description is given here. The purpose of the ACTIVE campaign was to characterize and understand the composition of the upper tropical troposphere. The campaign was based at Darwin, Australia, and was split into two phases. The first phase took place during November–December 2005 to study pre-monsoon convection such as the *Hector* thunderstorm and squall lines. The second phase took place during January–February 2006. During the second phase, an active monsoon occurred and by February it had completely subsided leaving a monsoon break where *Hectors* were once again observed. In this article we mostly use *in situ* data obtained from the first phase which sampled outflow cirrus that originated from the *Hector* thunderstorm, which forms over the Tiwi Islands during the transition from the wet to the dry season and during the break. The suite of *in situ* microphysical instrumentation that was deployed during ACTIVE on board the Egrett is summarized in Table I. The Stratton Park Engineering Company (SPEC) CPI instrument is described in Lawson *et al.* (2001). The CPI images ice crystals from about 5 μm upwards, however if the ice crystals are out of focus the 5 μm ice crystals will appear more like ∼15–30 μm in size. At these small sizes it is not possible for the CPI to distinguish ice crystal habit due to an inadequate pixel size of 2.4 μm. In this article, an algorithm is used to correct for oversizing and quantifying the probe sample volume, which is size-dependent as described in Connolly *et al.* (2007). To obtain a statistically meaningful representation of the PSD, the CPI averages the data to 10 s, and many of the 10 s PSDs are averaged together typically to 5 min, which reduces sampling errors significantly. The CPI was also operated in triggered mode which facilitates the measurement of the cirrus PSDs. In thick cirrus, this mode of operation can be considered as randomly sampling the ice in the cloud until good statistics of the PSD are built up. Moreover, in the paper by Connolly *et al.* (2007), it is shown that, when the corrections are applied, the CPI-measured PSDs are in good agreement with other microphysical probes. A suite of other probes on board the Egrett measured

humidity, ozone, turbulence and temperature and this payload is further described in Vaughan *et al.* (2008). The *in situ* parameters of fundamental importance to this article are the measured temperature, the CPI-estimated IWC and volume extinction coefficient. The *in situ* measured temperature and estimated IWC are used to generate the PSD using the parametrization described in Field *et al.* (2007). The CPI estimate of IWC has previously been described in Baran *et al.* (2009), but a brief description is given here.

The CPI estimate of IWC for this article is based on the effective density–size relationships found in Heymsfield *et al.* (2004); previously it was based on Heymsfield *et al.* (2002). Moreover, in the paper by Baran *et al.* (2009), the CPI estimate of IWC is compared against estimates using the 2D-C probe for a number of midlatitude cases and it is shown that the derived probability density functions (PDFs) of IWC using the two independent probes are statistically similar. The CIP estimate of IWC is also based on the density–size relationships described in Heymsfield *et al.* (2004). The CIP probe was corrected for shattering by filtering out any shattered artefacts using the particle interarrival times, as described in Field *et al.* (2006). However, shattering was minimal for ACTIVE due to the low flight speeds of the Egrett. It has been previously determined by Heymsfield *et al.* (2002) that the experimental uncertainty in the estimated IWC using imaging probes is likely to be ±50% due to errors in sampling volume, ice crystal shattering on the inlet of the probes (Field *et al.*, 2003; McFarquhar *et al.*, 2007; Heymsfield, 2007) and unknown ice crystal orientations. The CPI error in the measured cross-sectional area of each ice crystal is similarly ±50% due again to errors in the sampling volume, ice crystal shattering and unknown ice crystal orientations.

To test the ensemble model due to Baran and Labonnote (2007), five cases of semi-transparent tropical cirrus sampled during the ACTIVE campaign are used. These cirrus cases contrast fresh detached anvils, mature anvils, cirrus outflow and high-level cirrus; these cases are sufficiently different to be a good test of a generalized model of cirrus and the cases are described in Table II. It should be noted that in Table II the ranges of temperature for some cirrus cases are beyond the range of temperature upon which the PSD parametrization of Field *et al.* (2007) is based, and so for these cases any disagreement between model and CPI estimates could be due to lack of microphysical information at such extreme temperatures. Firstly, for two of the tropical cases described in Table II, the CPI and CIP measurements of the PSD are compared against each other in the next sub-section.

2.1. The measured particle size distribution function

In this section for the cases AE04 and AE06 the CPI and CIP-measured PSD, averaged over the whole flight whilst in cloud, are compared. These two cases have been chosen as they represent the full range of cirrus sampled by the Egrett, and the results of the comparisons are shown in Figure 2. Similar comparisons were performed for the other flights described in Table II but are not reproduced here for reasons of brevity, though results were found to be similar to those shown in Figure 2. Also shown in Figure 2 is the estimated PSD derived from the Field *et al.* (2007) parametrization using the CIP-estimated averaged IWC and the averaged

Table I. The suite of microphysical instrumentation deployed during the ACTIVE campaign showing the instrument, measured ice crystal size range and the measured quantities obtained by each instrument.

Instrument	Size range (μm)	Measurement or estimate
Cloud, Aerosol and Precipitation Spectrometer (CAPS)	0.5–1550	Size, number concentration
Cloud Particle Imager (CPI)	5.0–1800	Shape, size, number concentration, ice crystal shape, ice crystal cross-sectional area, IWC
Cloud and Aerosol Spectrometer (CAS)	0.5–50	Size, number concentration
Cloud Imaging Probe (CIP)	25.0–1550	Size, number concentration, IWC

Table II. The five cirrus cases sampled during the ACTIVE campaign showing the case number, date of sampling, the time in UTC (hour, minute, second: hhmmss) of the vertical profile (Pro) or transect (Trans), the type of cirrus, altitude of the transect or the profile bottom and profile top, and the measured in-cloud temperature.

Case	Date	Pro/Trans (UTC)	Cirrus type	Altitude (km)	Temperature (°C)
AE04	16 Nov 05	072732–091749	Fresh detached anvil diagonal transect.	13.0	−57.0
AE06	30 Nov 05	053822–060600	Thin Cirrus outflow edge of large anvil.	13.3–14.0	−59.3 to −65.3
AE08	3 Dec 05	091037–083846	Cirrus west outflow from large anvil.	11.6–13.8	−43.5 to −61.7
		065902–073111	Transect.	12.0	−48.0
AE10	5 Dec 05	074055–080217	High-level cirrus.	11.7–13.3	−45.0 to −57.9
AE21	27 Jan 06	065714–075031	Mature anvil remnant.	11.7–13.2	−44.2 to −55.9

in-cloud temperature, together with the $\pm$50% uncertainty in the parameterized PSD due to the uncertainty in the estimated IWC. Firstly, it can be seen from Figure 2(a) for the case AE04 that the CIP and CPI are generally within a factor 2 of each other, and both instruments exhibit some form of bi-modal structure at sizes just over 100 μm. However, for this particular case the CPI does generally measure more ice crystals than the CIP. In contrast, the Field *et al.* (2007) tropical parametrization does not exhibit such a strong bi-modal structure as the CIP or CPI. However, at sizes greater than about 80 μm, the upper uncertainty in the Field *et al.* (2007) tropical parametrization is generally within the CIP measurements. Since the ice crystal mass and particle extinction are both approximately proportional to the size squared, then from Figure 2 it can be seen that the maximum contribution to the particle extinction and ice crystal mass occurs at about 250 μm. At an ice crystal size of about 250 μm the figure shows that the Field *et al.* (2007) tropical parametrization is well within a factor of 2 or 3 of the CIP and CPI measurements, respectively. Interestingly, the Field *et al.* (2007) midlatitude parametrization exhibits a stronger bi-modal structure than the tropical parametrization, and it is shown in Figure 2 that the midlatitude parametrization, between the sizes of about 20 μm to less than 1000 μm, is within a factor of 2 of the CIP and CPI measurements. At sizes greater than about 1000 μm, the midlatitude parametrization falls off rapidly relative to the CIP measurements. Moreover, for ice crystal size greater than about 100 μm, the midlatitude PSD parametrization is within the uncertainty of the tropical parametrization.

The case AE06 is shown in Figure 2(b) and the results of comparison for the CPI and CIP are similar to Figure 2(a), except that for ice crystal sizes less than about 100 μm the CIP measures more ice crystals than the CPI, and the bi-modal structure for both instruments is less pronounced than in AE04. However, the figure generally shows that both the CIP and CPI measurements are within a factor of 2 of each other for ice crystal size less than about 800 μm. For this case the upper uncertainty of the Field *et al.* (2007) tropical parametrization is within the CIP and CPI measurements for ice crystal size greater than about 100 μm. At the ice crystal size of about 250 μm, where the maximum contribution to extinction and ice mass occurs, the PSD tropical parametrization is within about a factor of 2 of both the CIP and CPI measurements. Similar to Figure 2(a), the midlatitude PSD parametrization is generally well within a factor of 2 of the CIP and CPI measurements for ice crystal size less than about 500 μm, and at sizes greater than this the parametrization falls off rapidly relative to the CIP and CPI measurements. However, the midlatitude PSD parametrization is within the uncertainty of the tropical parametrization for ice crystal size between about 50 and 1000 μm.

Currently, there are uncertainties in the measurement of ice crystal number concentrations for ice crystal size less than about 200 μm due to errors in the probe sampling volume, ice crystal orientation and shattering. However, given the uncertainties, the CIP and CPI probes do agree with each other to generally within a factor of 2. From Figure 2, the uncertainty of $\pm$50% previously given to the CPI estimate of IWC and ice crystal cross-sectional area appears reasonable. Figure 2 also shows that the Field *et al.* (2007) PSD parametrizations are within a factor of 2 of the CIP or CPI measurements at ice crystal sizes of importance to the extinction and ice mass of the cloud. In the next sub-section, comparisons are made between the CIP and CPI estimates of IWC.
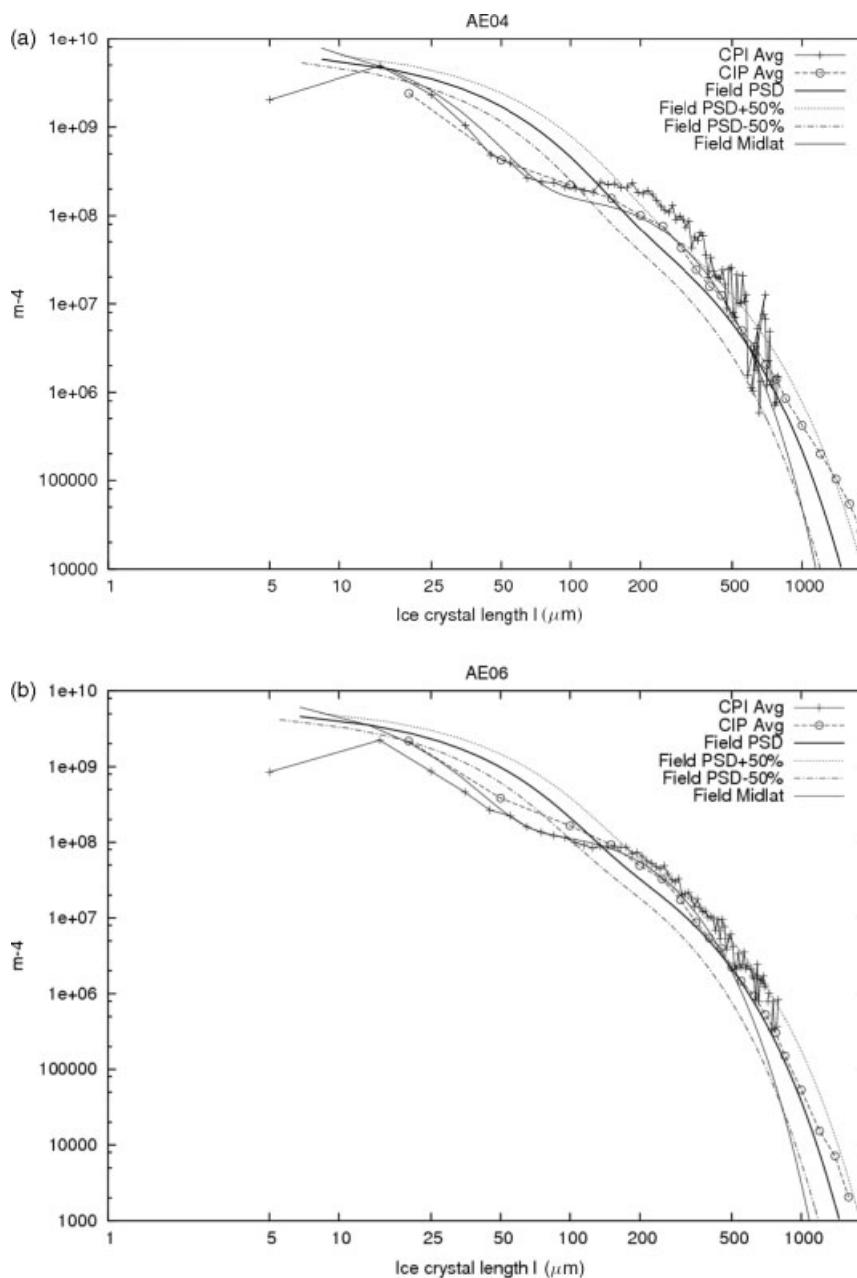
Figure 2. A comparison between the CPI (full lines with crosses), CIP (dashed lines with open circles) and Field *et al.* (2007) parametrizations of the ice crystal number density (m^{-4}) plotted against ice crystal length, l (μm), for the cases (a) AE04 and (b) AE06. The tropical (Field PSD) and midlatitude (Field Midlat) parametrizations are shown by the full bold line and thin full line, respectively. The $\pm$50% uncertainty in the Field tropical parametrization is represented by the dashed and dashed-dotted lines.

2.2. The CPI and CIP in situ estimated distribution of IWC

The CPI and CIP estimates of IWC for the cases AE04, AE06, and AE10 described in Table II are shown in Figure 3 as normalized PDFs. These are plotted as a function of estimated IWC in units of mg m^{-3}. These three cases were chosen as they represent the full range of cirrus sampled by the Egrett and results found for the other two cases were similar and are not reproduced here for reasons of brevity. For the case AE04 (Figure 3(a)), the mean IWCs found from the CPI and CIP estimates were 96.02 and 120.09 mg m^{-3}, respectively, which are well within a factor of 2 of each other. Moreover, from Figure 3(a) the midpoint bin modal values of IWC for the CPI and CIP are 21 and 66 mg m^{-3}, respectively, and between 0.66 and 2100 mg m^{-3} the two distributions appear to be similar. However, there is a low

IWC bias for the CPI between 0.021 to 0.21 mg m^{-3}, which is likely due to the CIP processing not being optimised for low particle concentration data. This low IWC bias represents only 5% of the total IWC distribution, and so it is not expected to have a significant impact on the rest of this article.

The case AE06 is shown in Figure 3(b) and interestingly, in contrast to Figure 3(a), the CIP and CPI IWC distributions are biased to lower IWC values, though for IWCs greater than midpoint bin values of 21 mg m^{-3} the CIP probe estimates more IWC than the CPI. As a result of this shift in the CPI and CIP IWC PDFs, the mean IWC values found for each distribution were 4.10 and 24.12 mg m^{-3}, respectively, about a factor of 6 difference between the CPI and CIP estimates for this case. Moreover, from Figure 3(b) the midpoint bin modal values of IWC for the CPI and CIP
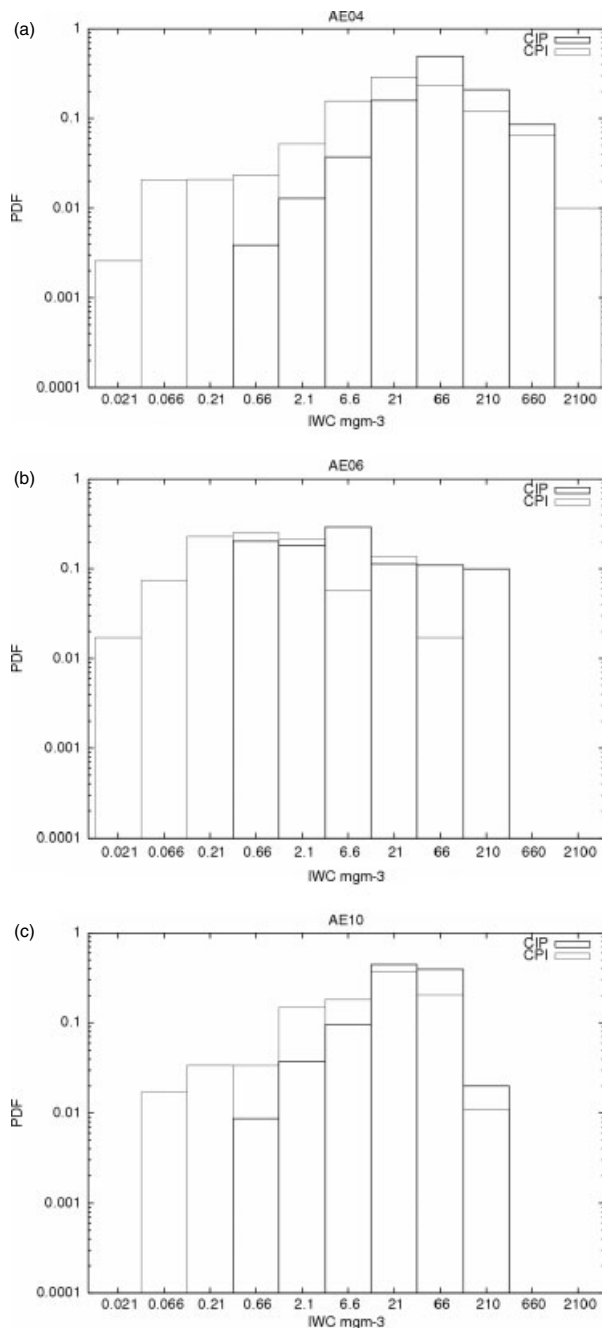
Figure 3. The CPI (thin boxes) and CIP (bold boxes) normalized probability distribution functions (PDFs) plotted as a function of IWC (mg m^{-3}) for the tropical cirrus cases (a) AE04, (b) AE06, and (c) AE10.

Table III. The Mann–Whitney U test applied to the cases AE04, AE06 and AE10.

Case	n_1[a]	n_2[a]	U-statistic	$P \geq 0.05$[b]	$H_0(95\%)$
AE04	11	7	54.0	0.18	Proved
AE06	8	6	39.0	0.059	Proved
AE10	8	6	31.5	0.34	Proved

[a]n_1 and n_2 are the populations for the CPI and CIP distributions, respectively.
[b]$P \geqslant 0.05$ is the two-tailed test and therefore H_0 is the null hypothesis at the 95% confidence level.

test. This statistical test quantifies whether two distributions measured by independent instrumentation originate from the same distribution. For this article, the null hypothesis (H_0) is that the CPI- and CIP-estimated IWC PDFs are the same. The results of the Mann–Whitney U test applied to the cases AE04, AE06, and AE10 are summarized in Table III. It can be seen that the null hypothesis at the 95% confidence level is proved for all three cases, which means that, at least statistically, the IWC distributions derived from the CPI and CIP probes are not significantly different. However, the case AE06 does not pass the test as strongly as the other two cases.

Given that the CPI and CIP IWC distributions are not significantly different this means that the CPI estimated IWC can be used with confidence in testing the ensemble model prediction of IWC. In the next sub-section the observed ice crystal shape distributions are discussed.

2.3. The observed ice crystal shape distributions

The ice crystal shape distributions for each of the cases described in Table II were determined using the shape recognition algorithm that comes standard with the CPIView image processing software. The ice crystal shape distribution determined using CPIView for each case is shown in Figure 4. It should be noted here that there are limitations to the CPI auto-classification algorithm since the CPI cannot distinguish ice crystal shapes below a size of about 35 μm, and these may appear as 'quasi-spherical' in the images due to diffraction caused by the limiting resolving power of the instrument, so these particles may appear sufficiently regular not to be characterized by the software as small irregulars. Moreover, the small irregulars may still not be a satisfactory classification as these too may still not be sufficiently resolved to reveal their true geometries. As noted by Stoelinga *et al.* (2007), such classifications as 'quasi-spherical' and/or 'irregular' should really be classified as 'indeterminate'.

The common feature from Figure 4 is that for all five cases the most common habits are the small irregulars and 'quasi-spherical' ice crystals. From Figure 4, for each of the cases, the 'quasi-spherical' and small irregular ice crystals account for about 80% of the shape distributions with big irregulars contributing between about 10% to15% and the pristine shapes such as single hexagonal columns and single hexagonal plates contributing less than about 5% to the ice crystal populations. The small irregular or big irregular ice crystals may themselves be composed of plate or hexagonal column components. However, the largest single contribution to the shape distribution for all five cases is provided by the small irregular ice crystals which contribute between about 43% to almost 60% to the shape distribution.
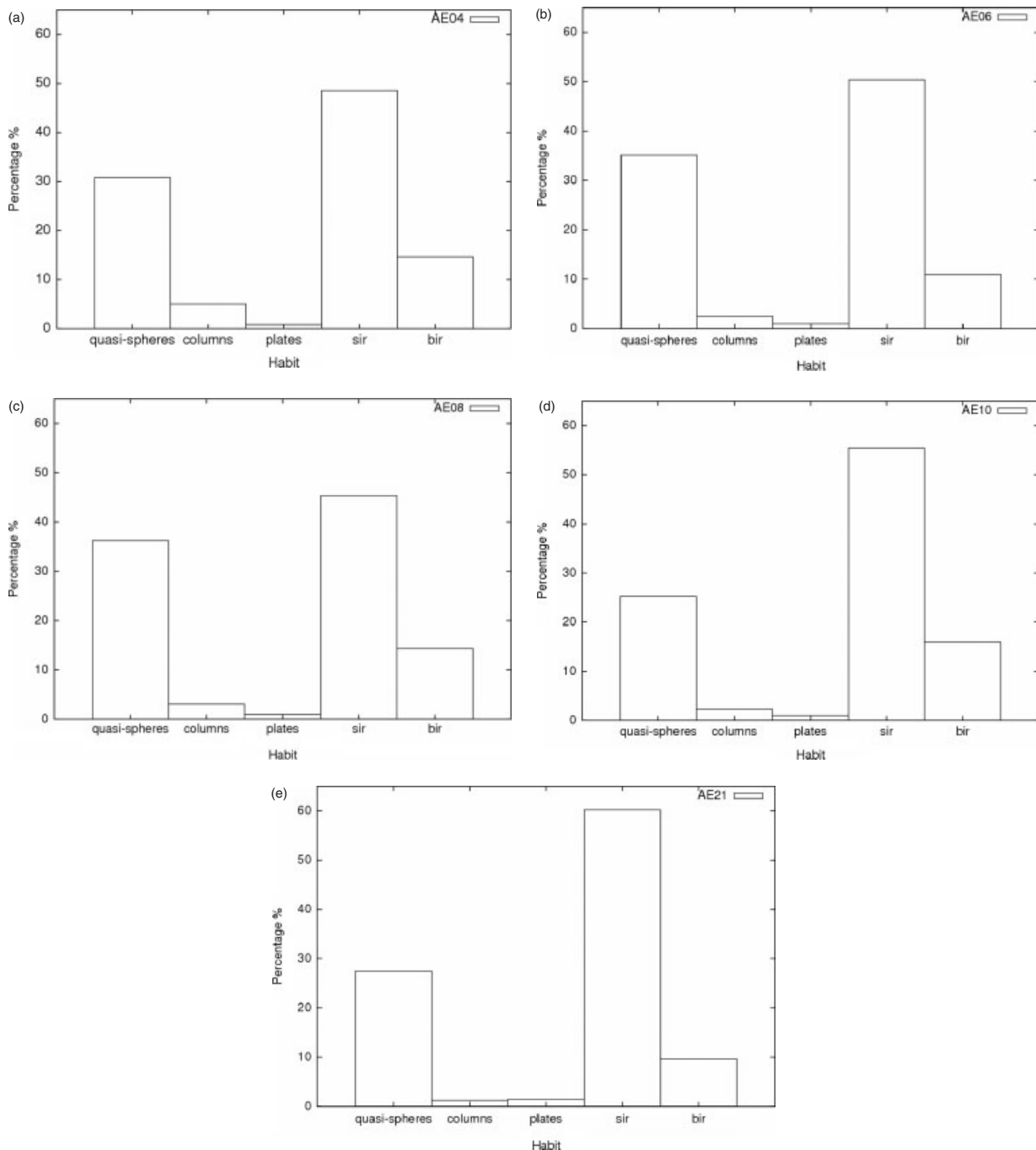
are 0.66 and 6.6 mg m^{-3}, respectively. Of all the five flights, AE06 represents the lowest IWC case and as such there are likely to be issues surrounding the probes' sampling volumes. This case is examined in more detail in section 4.3 of this article.

In contrast to AE06, the IWC PDFs estimated from the CIP and CPI instruments are shown in Figure 3(c) for the case AE10. It can be seen that the two PDFs agree fairly well for midpoint bin values greater than 0.21 mg m^{-3} and the midpoint bin modal value is 21 mg m^{-3} for both the CPI and CIP probes. The mean estimated IWC values found for the CPI and CIP probes were 20 and 32.73 mg m^{-3}, respectively, well within a factor of 2 of each other.

A more quantitative assessment of the CIP and CPI IWC PDFs can be obtained from the statistical Mann–Whitney U

Figure 4. The percentage distribution of ice crystal shapes as determined by the CPI shape recognition algorithm for the tropical cirrus cases (a) AE04, (b) AE06, (c) AE08, (d) AE10, and (e) AE21. The ice crystal shapes are classified as quasi-spheres, hexagonal ice columns (columns), hexagonal ice plates (plates), small irregulars (sir) and big irregulars (bir).

The quasi-spherical ice crystals are the second most common crystal type, contributing approximately 25% to 35% to the shape distribution.

CPI ice crystal images obtained from the tropical cirrus cases AE04, AE08 and AE21 are shown in Figures 5–7 and these ice crystal images correspond to each of the transects and profiles described in Table II. Ice crystal images obtained from the cases AE06 and AE010 are similar and are not shown for reasons of brevity. Ice crystal images obtained from the diagonal transect across the fresh anvil AE04 are shown in Figure 5. The images show that for this case there is evidence of large plate aggregates which have previously been reported by Connolly *et al.* (2005) and Um and McFarquhar (2009). These large plate-aggregates can

also be accompanied by smaller indeterminate ice crystals and ice crystals which appear 'quasi-spherical'. As pointed out by Um and McFarquhar (2009), although these plate aggregates may not be the most common type of ice crystal in the shape distribution they can, due to their large cross-section, significantly contribute to the bulk extinction of the cloud. The maximum dimensions of the plate-aggregates shown in Figure 5 for this particular case can range between ∼250 and almost 500 μm. Figure 6 shows images obtained from case AE08 and again these show evidence of large aggregated ice crystals accompanied by indeterminate ice crystals as well as 'quasi-spherical' ice crystals. For AE08 the images begin at 1651 (local time), corresponding to the profile bottom at an altitude of ∼12 km; as can be seen from

Figure 6, at this altitude the ice crystal shapes range from 'quasi-spherical' of maximum dimensions less than ∼55 μm to large ice crystal aggregates of maximum dimensions of several hundred microns. The images obtained at 1839 (local time) correspond to near the profile top (altitude almost 14 km) and at this altitude the ice crystals consist of large and small indeterminate irregular ice crystals. Ice crystal images obtained from the mature anvil case AE21 (Figure 7) at 1627 (local time) correspond to near the profile bottom (altitude ∼11.7 km). At this altitude the ice crystals appear indeterminate irregular and aggregated; some rosettes appear and a few 'quasi-spherical' ice crystals. More rosette crystals appear at 1714 (local time) at altitude ∼12.6 km and these are more discernible as rosettes compared to the previous images, with evidence of air inclusions in some of the component branches. The rosettes in the shape-recognition algorithm could well be classified as small irregular or big irregular ice crystals depending on their size. This mature anvil case is in contrast to the fresh anvil case of AE04 where no rosettes were visible in those ice crystal images shown in Figure 5. At close to the profile top at 1720 (local time), corresponding to an altitude of almost 14 km, the ice crystals appear smaller than the previous images shown for this case with the appearance of more 'quasi-spherical' ice crystals and indeterminate irregulars, though some smaller rosettes are still discernible at close to the profile top.

Figure 4 demonstrated that most of the ice crystal shapes consisted of 'quasi-spherical', small and large irregular ice crystals. However, on closer inspection of Figures 5–7, the actual geometrical shapes of these small irregular and large irregular ice crystals may differ significantly from each other. The large irregulars might consist of aggregated plates to rosettes, while the small irregulars might consist of rosettes to more indeterminate ice crystal shapes. With such an array of ice crystal shape, the five cases presented in Table II should provide a rigorous test for the ensemble model combined with the PSD parametrization. In the next section, the macrophysical and microphysical properties to be tested are defined.

3. Macrophysical and microphysical definitions

As previously described in section 1, the parametrized PSD is generated from the CPI estimated IWC, discussed in subsection 2.2, and the measured in-cloud temperature. This parametrized PSD is independent of ice crystal shape. The parametrized PSD is then applied to the ensemble model of Baran and Labonnote (2007) and, upon integration over this shape distribution, the quantities IWC and volume extinction coefficient are predicted. The ensemble model prediction of IWC is provided by

$$\text{IWC} = \int \rho_e(\Delta) n(\Delta) V(\Delta) \mathrm{d}\Delta, \qquad (1)$$

where the vector Δ represents the ensemble shape distribution as a function of maximum dimension. The terms $V(\Delta)$ and $n(\Delta)$ are the geometric volume of ice crystals and the ice crystal number concentration over the shape distribution as a function of ice crystal maximum dimension, respectively. The ice crystal number concentration is predicted by the PSD scheme. The term $\rho_e(\Delta)$ is the ensemble model effective density relationship

and is defined as

$$\rho_e(\Delta) = \frac{V(\Delta)}{V_s(\Delta)} \rho_i, \qquad (2)$$

where $V_s(\Delta)$ is the volume of the circumscribing sphere and ρ_i is the bulk density of ice assumed to be 0.92 g cm^{-3}. To obtain a general ensemble model effective density–size relationship that can be applied to Eq. (1), $\rho_e(\Delta)$ was evaluated for each ensemble member for a given maximum dimension and the best fit to Eq. (2) was found using

$$\rho_e(D) = \frac{aD}{b+D} + \frac{cD}{d+D} + eD + f, \qquad (3)$$

where the maximum dimension (D) is in units of μm and the coefficients $a, b, c, d, e,$ and f are given by 10.196, 100.566, −10.818, 768.346, −4.399 × 10^{-5} and 1.199, respectively.

A comparison between the best fit Eq. (3) and $\rho_e(\Delta)$ plotted as a function of ice crystal maximum dimension is shown in Figure 8; also plotted in the figure are the Brown and Francis (1995), Wilson and Ballard (1999) and Heymsfield *et al.* (2004) (HM04) effective density–size relationships. The HM04 parametrization of the effective density–size relationship is derived from *in situ* data obtained in the Tropics and midlatitudes. To compare with the ensemble model effective density–size relationship, the HM04 tropical parametrization is used but using the upper and lower limits of the best fitted area–size relationship given in Figure B1 of HM04. Figure 8 shows that for maximum dimensions less than about 100 μm, compared to the ensemble model the other three parametrizations predict an effective density that can significantly exceed unity (though in practice the density is limited so that they never exceed unity). However, for maximum dimensions between about 100 and 1300 μm, all effective density–size parametrizations are within about a factor of 2 of each other. Moreover, in this size range the parametrized ensemble model ρ_e agrees best with Wilson and Ballard (1999) and the upper limit of the Heymsfield *et al.* (2004) ρ_e. For ice crystal maximum dimensions from about 1600 to 8000 μm, Eq. (3) fits between the ensemble model points, due to a local maximum in Eq. (2) at about 4000 μm. This local maximum in Eq. (2) is caused by the more compact five-branched ensemble member shown in Figure 1(d). At maximum dimensions greater than about 1300 μm, the differences between the ensemble model effective density–size parametrization and the other parametrizations exceed a factor of 2. However, at such large maximum dimensions the ice crystal number concentration will generally be very small and as a consequence the contribution of these large ice crystals to the integrand of Eq. (1) will be insignificant. Throughout the rest of this article, Eq. (3) is applied to Eq. (1) to predict the ensemble model IWC.

From the derived IWC, the IWP (g m^{-2}) is defined as:

$$\text{IWP} = \int_{z_1}^{z_2} IWC(z) \mathrm{d}z, \qquad (4)$$

where z_1 and z_2 are the cloud bottom and cloud top, respectively, as defined by the aircraft.

The CPI does not directly determine the volume extinction coefficient, and as a result this quantity must
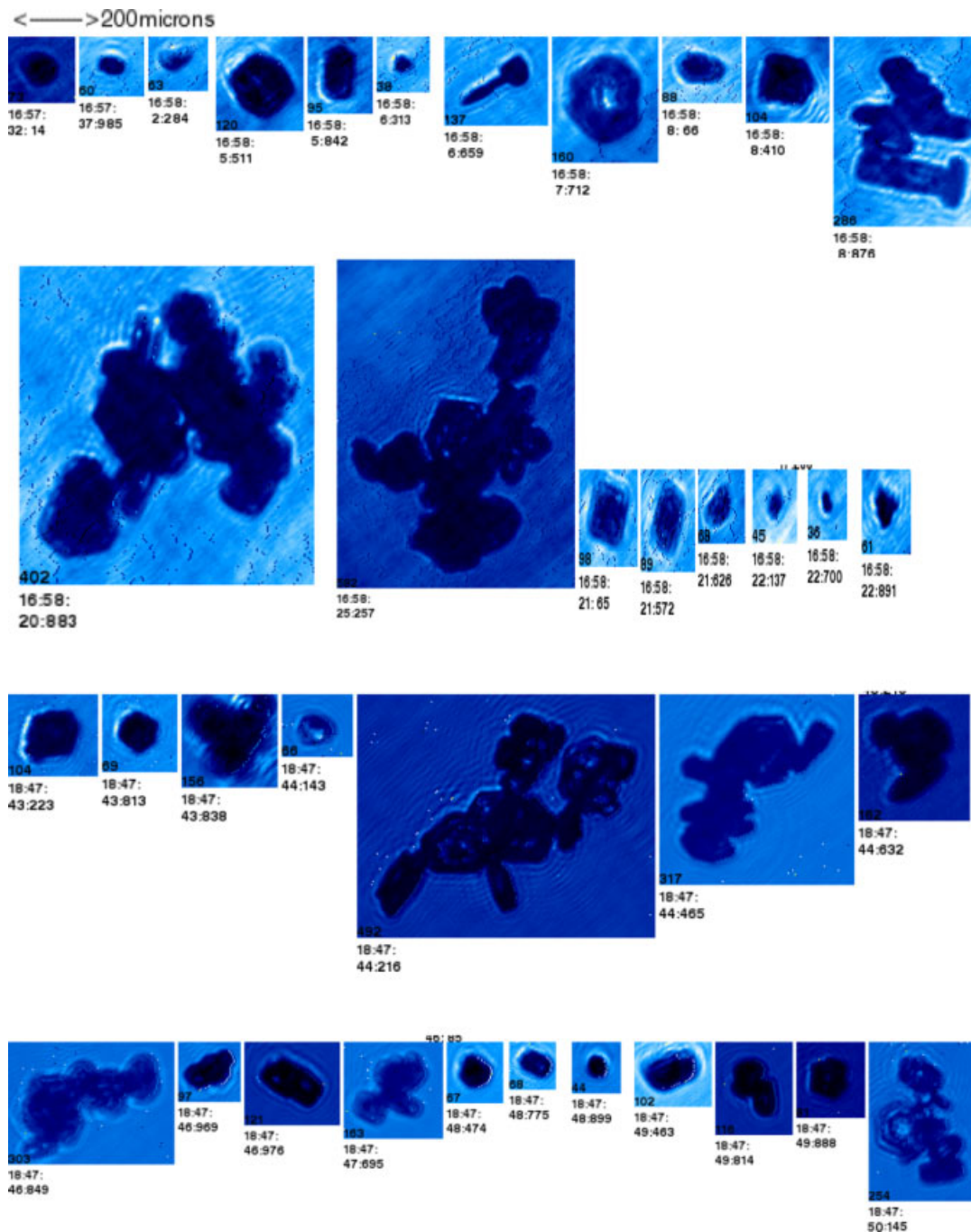
Figure 5. CPI images of the ice crystal shapes obtained during the straight and level run through AE04. The scale is shown at the top left, and the size of ice crystal (μm) is embedded in each image. The local time (hr:min:sec.sec) is shown below each image This figure is available in colour online at wileyonlinelibrary.com/journal/qj

be determined from the measured ice crystal total cross-sectional area of the ice crystal population per unit volume, assuming the limit of geometric optics to be valid. A further assumption is that the population of ice crystals is randomly oriented in space, so the volume extinction coefficient in the limit of geometric optics is given by

$$\sigma(\Delta) = 2 \int n(\Delta) < A(\Delta) > \mathrm{d}\Delta \tag{5}$$

where the factor 2 comes from the fact that, in the limit of geometric optics, the volume extinction is twice the orientation-averaged geometric cross-section $<A(\Delta) >$ (van de Hulst, 1957). The volume extinction coefficient

predicted by the ensemble model is determined in exactly the same way as given by Eq. (5).

Since the limit of geometric optics is applicable to solar wavelengths, then the total solar optical depth, τ, is given by:

$$\tau = \int_{z_1}^{z_2} \sigma(z)\mathrm{d}z. \tag{6}$$

In the next section, the ensemble model predictions of Eq. (1), (4)−(6) are compared against the CPI *in situ* estimates of the same quantities for all five cases of tropical cirrus described in Table II.
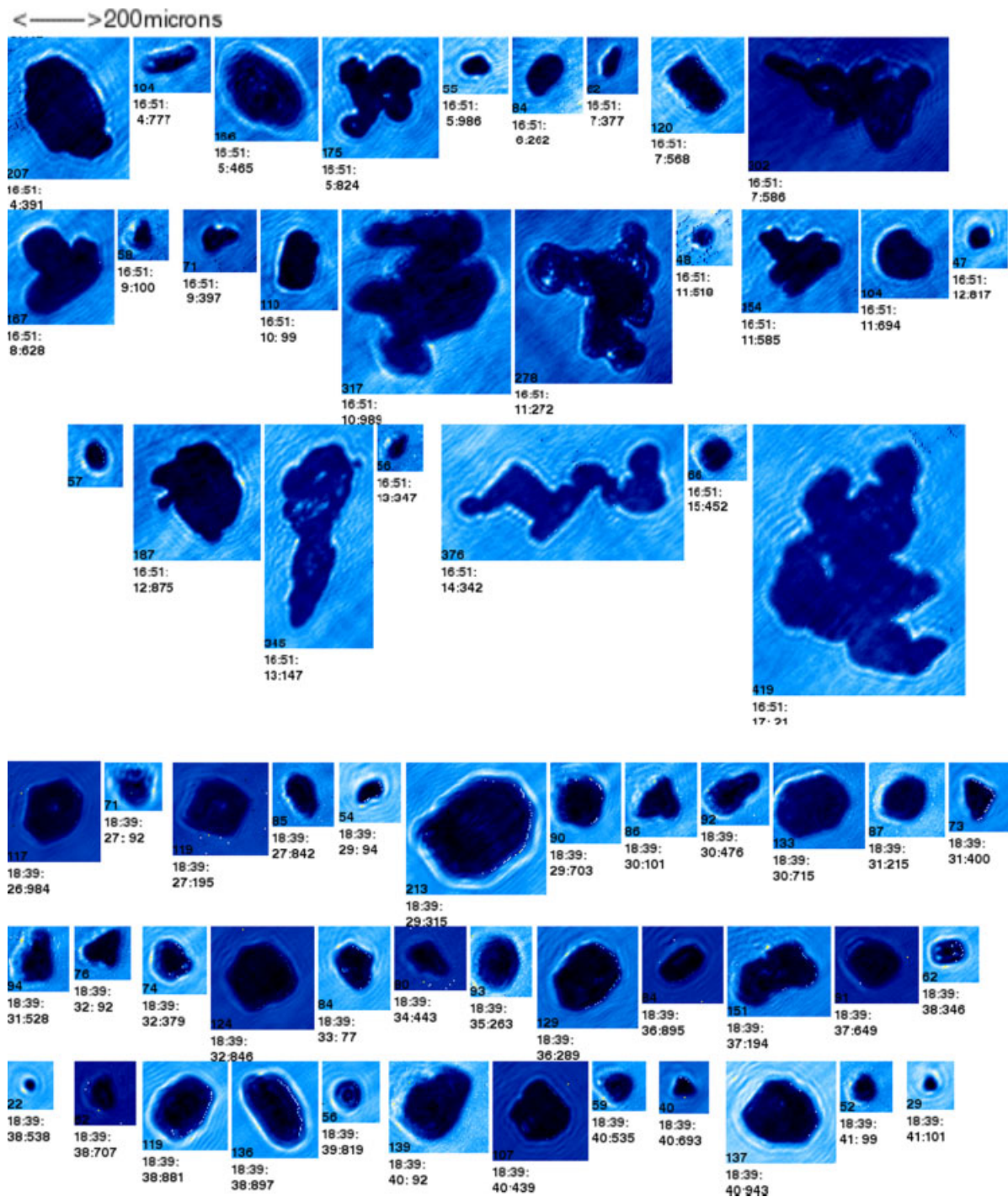
Figure 6. As Figure 5, but for the case AE08, with the images showing the profile ascent from top left to bottom right This figure is available in colour online at wileyonlinelibrary.com/journal/qj

4. Comparing *in situ* CPI estimates of the macrophysical and microphysical properties of tropical cirrus against ensemble model predictions

In this section the predictive value of the ensemble model of cirrus ice crystals due to Baran and Labonnote (2007) combined with the Field *et al.* (2007) PSD parametrization is further examined for the case of semi-transparent tropical cirrus. The ensemble model predictions of IWC, IWP, the volume extinction coefficient and the total solar optical depth are compared against CPI estimates of these quantities. In section 2 the experimental uncertainties in the CPI estimates of IWC, and volume extinction coefficient were

stated as ±50%. Likewise the CPI error in the derived IWP and total solar optical depth will also be ±50%, neglecting errors determining cloud top and cloud base. The uncertainties in the ensemble model predictions of the IWC, IWP, volume extinction coefficient and the total solar optical depth are based upon the error in the CPI-derived IWC. This ±50% uncertainty approximately propagates through the parametrized PSD (Field *et al.*, 2007) and so will consequently define the uncertainty in the ensemble model predictions.

To obtain meaningful comparisons between the ensemble model combined with the PSD parametrization predictions and the CPI *in situ* estimates of the macrophysical and
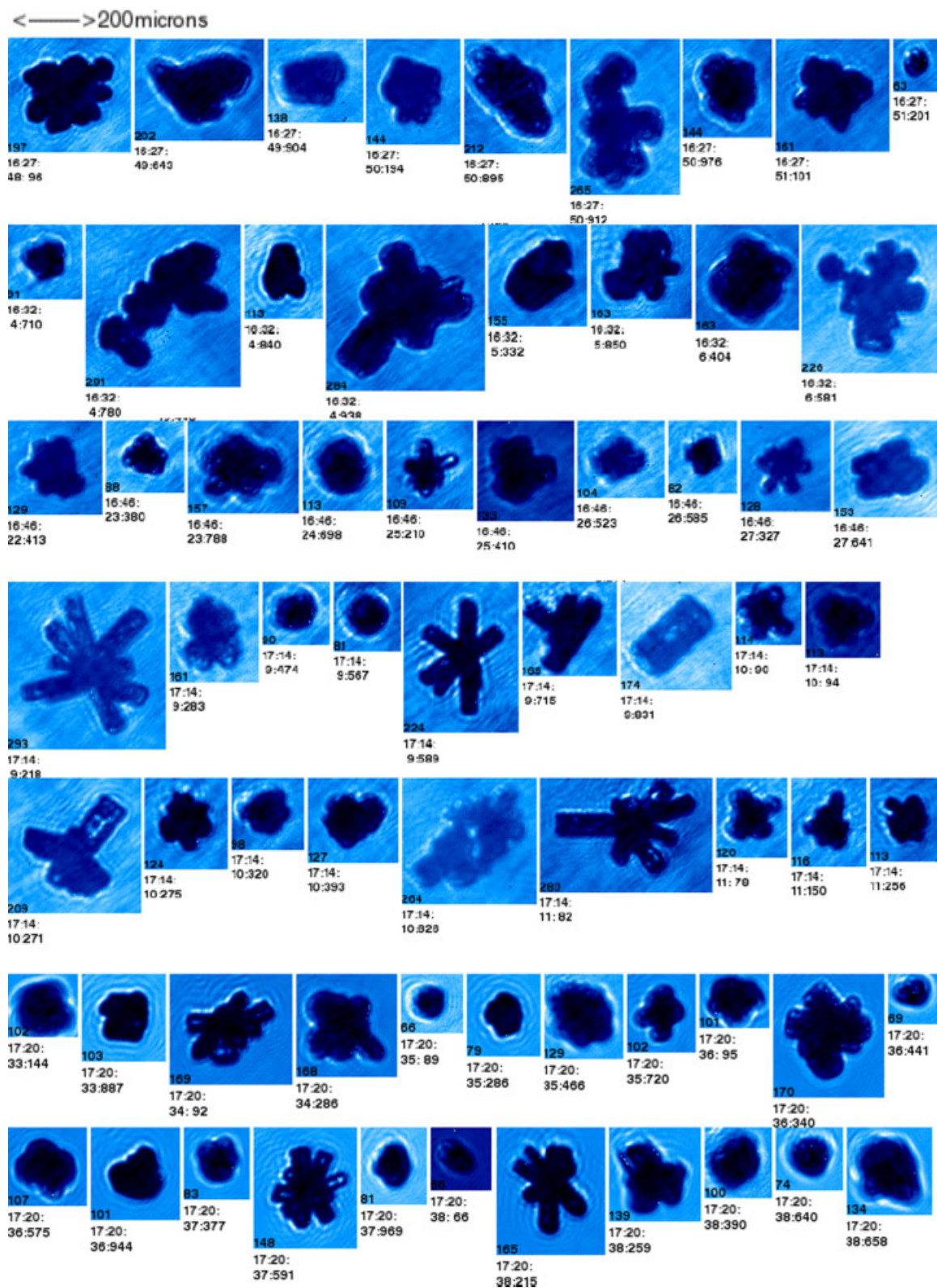
Figure 7. As Figure 6, but for case AE21 This figure is available in colour online at wileyonlinelibrary.com/journal/qj

microphysical properties of tropical cirrus, the transects and profiles described in Table II were averaged. For all the cases, it was found that, in order to remove high-frequency variations that were present in the data, a running mean of 10 s was required before meaningful comparisons could be made between the ensemble model predictions and CPI estimates.

4.1. Comparing ensemble model predictions of IWC and IWP against CPI estimates

In this section the ensemble model effective density-size parametrization given by Eq. (3) is combined with the PSD scheme to predict the IWC. The ensemble model predicted IWC is compared against the CPI estimates for all cases described in Table II. The ensemble model prediction of
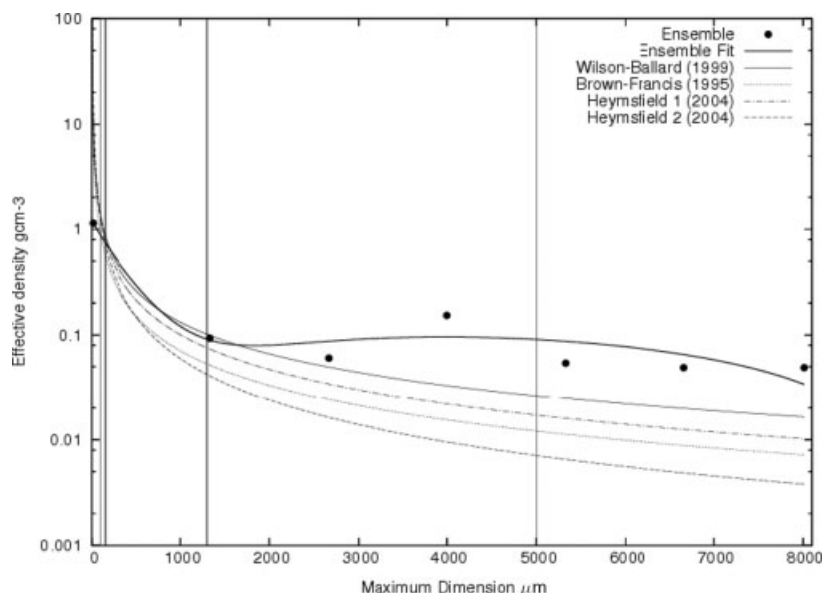
Figure 8. The effective density (g cm^{-3}) plotted against ice crystal maximum dimension (μm) for each member of the ensemble using Eq. (2) (filled circle), the best-fit line to Eq. (2) (bold line), and the effective density–size relationships of Brown and Francis (1995; dotted line), Wilson and Ballard (1999; grey line) and Heymsfield *et al.* (2004). Heymsfield 1 (dash-dotted line) and Heymsfield 2 (dashed line) represent the upper and lower values assumed for the effective density–size relationships, respectively. The bold and grey vertical lines plotted represent the limits of measured ice crystal maximum dimension for the Brown and Francis (1995) and Heymsfield *et al.* (2004) effective density parametrizations, respectively.

IWP is also compared against the derived CPI estimate using Eq. (4) applied to the vertical profiles obtained for the cases AE06, AE08, AE10 and AE21. In the figures that follow all times are expressed in terms of Universal time (UTC). Firstly, comparisons are made between the ensemble model predictions and CPI estimates of IWC for the cases AE04 and AE08 in which straight and level transects were flown.

The results of this first comparison using the cases AE04 and AE08 are shown in Figure 9(a) and (b), respectively. The ensemble model uncertainty in the prediction of IWC was estimated as being about ±55%. In Figure 9(a), which shows results for the fresh anvil case, it can be seen that the CPI-estimated IWC reaches a maximum of about 1 g m^{-3} at approximately 0734 UTC, then decreases to about 0.05 g m^{-3} at about 0814 UTC and increases again to about 0.1 g m^{-3} at about 0854 UTC; thereafter the CPI-estimated IWC generally decreases to about 0.007 g m^{-3} by the end of the transect. In comparing the ensemble model prediction of IWC with the CPI estimate, the figure shows that the range in the ensemble model uncertainty tends to overlap with the CPI uncertainty for all cases considered.

Results of comparing the ensemble model predictions against the CPI estimates of IWC for the straight and level transect flown through AE08 is shown in Figure 9(b). The figure shows that the CPI estimated IWC also reaches a maximum of about 1 g m^{-3} in the middle of the transect and then falls off to about 0.002 g m^{-3} at the beginning and end of the transect. The results shown in Figure 9(b) are very similar to Figure 9(a).

Results of comparing the ensemble model prediction of IWC against the CPI estimates of IWC for the vertical profiles described in Table II are shown in Figure 10(a)–(d). The case AE06 is shown in Figure 10(a) and this case, as discussed in section 2.3, has the lowest averaged IWC of all the cases. The figure shows that the vertically averaged IWC varies between about 0.01 g m^{-3} at profile bottom to about 0.0002 g m^{-3} at profile top. For this geometrically thin tropical cirrus case, the figure shows that the upper range of the uncertainty in

the ensemble model prediction of IWC tend to generally overlap with the lower range of the CPI uncertainty for six out of the seven altitudes considered. At profile top (altitude of $\sim$ 14 025 m), the uncertainty in the ensemble model prediction does not overlap with the CPI uncertainty.

For case AE08 (Figure 10(b)), it can be seen that for all altitudes the upper range of the uncertainty in the ensemble model prediction of IWC generally lies within the lower range of the CPI experimental uncertainty. Results of comparison for AE10 are shown in Figure 10(c), and the uncertainty in the ensemble model prediction of IWC generally tend to overlap with the CPI uncertainty for all altitudes considered. The case AE21 (Figure 10(d)) shows results similar to Figure 10(c).

The ensemble model-predicted IWP using Eq. (4) applied to the vertical profiles shown in Figure 10(a)–(d) is shown in Table IV together with the CPI-estimated IWP. The table shows that for all cases the ensemble model does predict an IWP uncertainty that is within the uncertainty of the CPI estimates. However, the ensemble model IWP does tend to be within the lower range of the CPI uncertainty for case AE06. For cases AE08, AE10 and AE21 there is good overlap between the ensemble model uncertainty and the CPI uncertainty.

In the next sub-section, the ensemble model predictions of the volume extinction coefficient and the total solar optical depth are compared against the CPI estimates for all the cases described in Table II.

4.2. Comparing the ensemble model predictions against CPI estimates of the volume extinction coefficient and the total solar optical depth

In this sub-section the ensemble model of Baran and Labonnote (2007) combined with the PSD scheme is used to predict the volume extinction coefficient and the total solar optical depth using Eqs. (5) and (6), respectively. These predictions and the associated uncertainty are compared
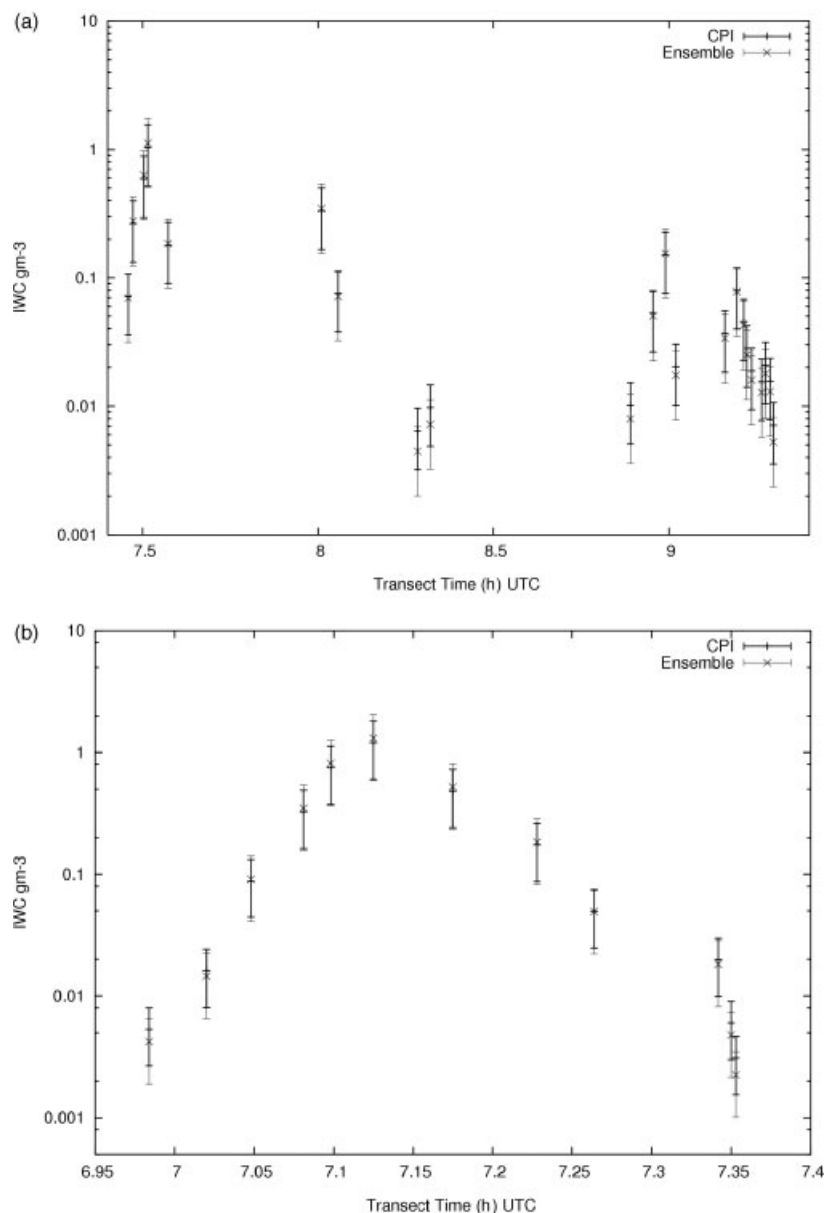
Figure 9. The CPI-estimated IWC and the ensemble model predictions as a function of time (UTC) obtained during the straight and level run through the cases (a) AE04 and (b) AE08, with the experimental uncertainty of the CPI estimate shown as the bold error bar labelled CPI. The ensemble model uncertainty is shown as the grey error bar labelled Ensemble.

Table IV. Comparison of the ensemble model prediction of IWP with the CPI-estimated IWP for the integrated vertical profiles shown in Figure 10(a)−(d).

CASE	CPI (gm^{-2})	Ensemble (gm^{-2})
AE06	1.019 ± 0.51	0.67 ± 0.37
AE08	7.799 ± 3.90	6.10 ± 3.40
AE10	34.99 ± 17.50	32.44 ± 17.84
AE21	29.84 ± 15.0	27.33 ± 15.03

against the CPI estimates of the same quantities derived using the same equations for all the tropical cirrus cases described in Table II.

The results of comparison between the ensemble model predictions and CPI estimates of the volume extinction coefficient are shown in Figure 11(a) and (b) for the straight and level transects flown in the cirrus cases AE04 and AE08, respectively. Figure 11(a) shows that the uncertainty in the ensemble model predictions when combined with the PSD scheme overlaps the uncertainty in the CPI estimates for all 27 cases. Therefore, there is good agreement between the ensemble model prediction and the CPI estimate. The case AE08 is shown in Figure 11(b) which shows that the results are very similar to Figure 11(a) for all 12 cases.

Note that, in regions of highest IWC in Figure 11(a), the volume extinction coefficient reaches about 0.025 m^{-1} for the given CPI IWC at about 0734 UTC. In the regions of lowest IWC at the end of the transect, it can be seen that the volume extinction coefficient is about 0.0003 m^{-1} for the given CPI IWC. Clearly, in the regions of highest IWC, the ensemble model or any other model would have no impact on the radiative balance of cirrus in these regions since the optical depth is so large. However, in the regions of moderate to low IWC, the transmissions are large and so it is more important that in these regions the ensemble model
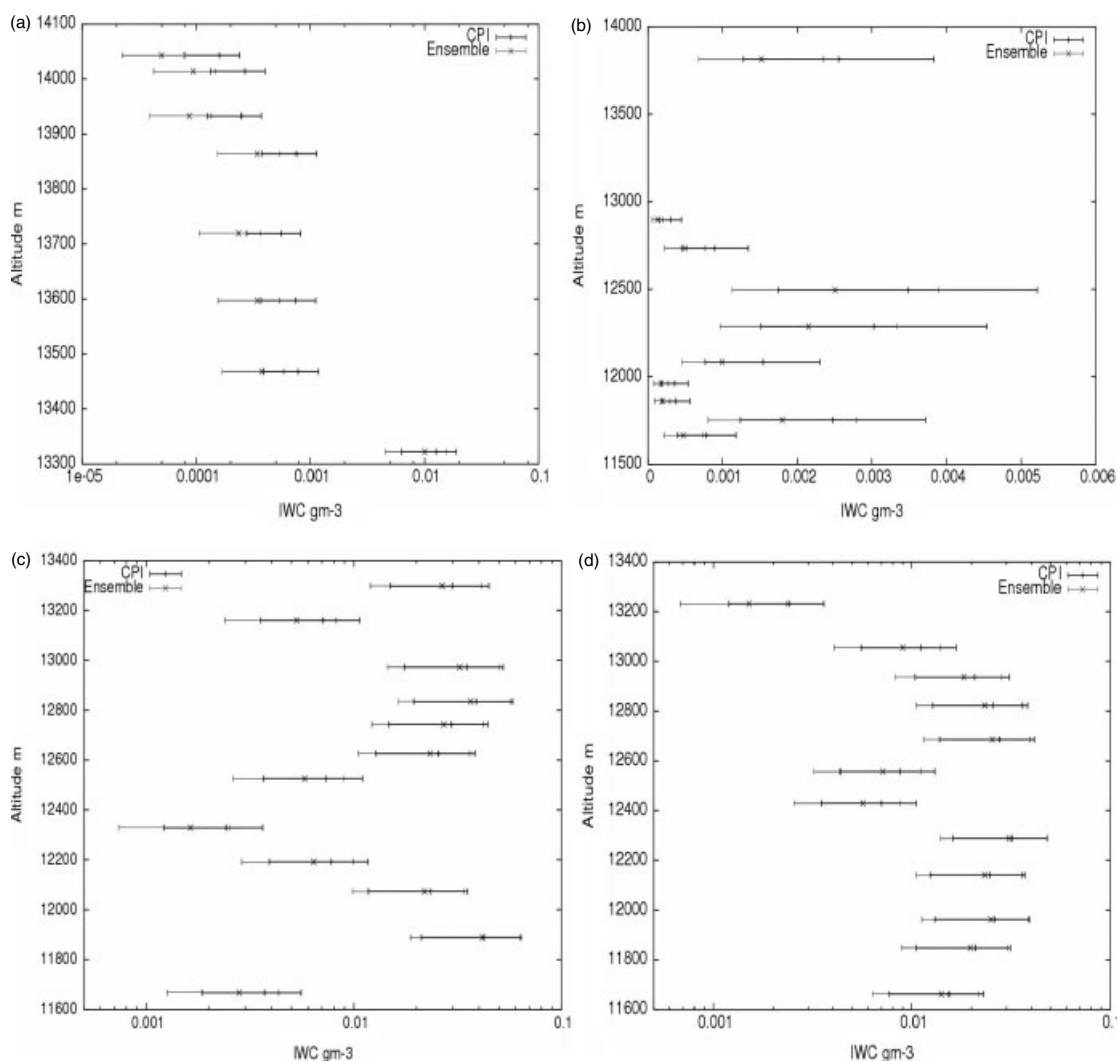
Figure 10. The ensemble model-predicted IWC and the CPI-estimated IWC plotted as a function of altitude for the cases (a) AE06 (b) AE08 (c) AE10 and (d) AE21. The experimental uncertainty of the CPI estimate is shown as the bold error bar labelled CPI. The ensemble model uncertainty is shown as the grey error bar labelled Ensemble.

or any other model predicts a volume extinction coefficient for a given IWC that is within the uncertainty of the CPI estimates for the purpose of helping to improve the cirrus radiative balance within GCMs. This still does not mean that the high IWC regions can be ignored from the point of view of ice crystal modelling, as it is still important to accurately simulate the IWC in these regions for the purposes of IWC retrievals from space (Waliser *et al.*, 2009).

In Figure 12(a)−(d), the ensemble model uncertainty in the prediction of the volume extinction coefficient is shown, together with the CPI uncertainty as a function of altitude for the cases AE06, AE08, AE10, and AE21, respectively. From Table IV, cases AE06 and AE08 have the lowest IWP according to the CPI estimates of about 1 and 8 g m^{-2}, respectively. For these two cases of low IWP, it can be seen from Figure 12(a) and (b) that the upper range of the ensemble model uncertainty tends to be either just within the lower range of the CPI uncertainty or just outside that uncertainty. This is in contrast to Figure 11(a) and (b). One of the possible reasons for this, in the case of AE06, is that the temperature range of this profile is outside the range of applicability of the PSD scheme. However, case AE08, as can be seen from Table II, does not generally lie outside the range of temperature for which the PSD scheme can

be considered valid. The physical reasons for the ensemble model uncertainty being either just outside or within the lower range of the CPI uncertainty is further explored in a later section.

The uncertainty in the ensemble model predictions of the volume extinction coefficient for cases AE10 and AE21 are shown in Figure 12(c) and (d), respectively. For case AE10, the ensemble model uncertainty does more generally overlap the CPI uncertainty relative to Figure 12(a) and (b) for all 12 altitudes, though the upper uncertainties of the ensemble model do tend to lie within the lower range of the CPI uncertainty. The ensemble model results for case AE21 (Figure 12(d)) are similar to Figure 12(c).

From the ensemble model predictions and CPI estimates of the vertical profiles of volume extinction coefficient shown in Figures 12(a)−(d), the total solar optical depth is found by applying Eq. (6) to those profiles. The results of comparing the ensemble model predictions and CPI estimates of the total solar optical depth together with the model and experimental uncertainties are summarised in Table V. The table shows that the uncertainty in the ensemble model prediction of the total solar optical depth for cases AE06 and AE08 is not within the experimental uncertainty of the CPI estimates for both those cases. However, Table V does show
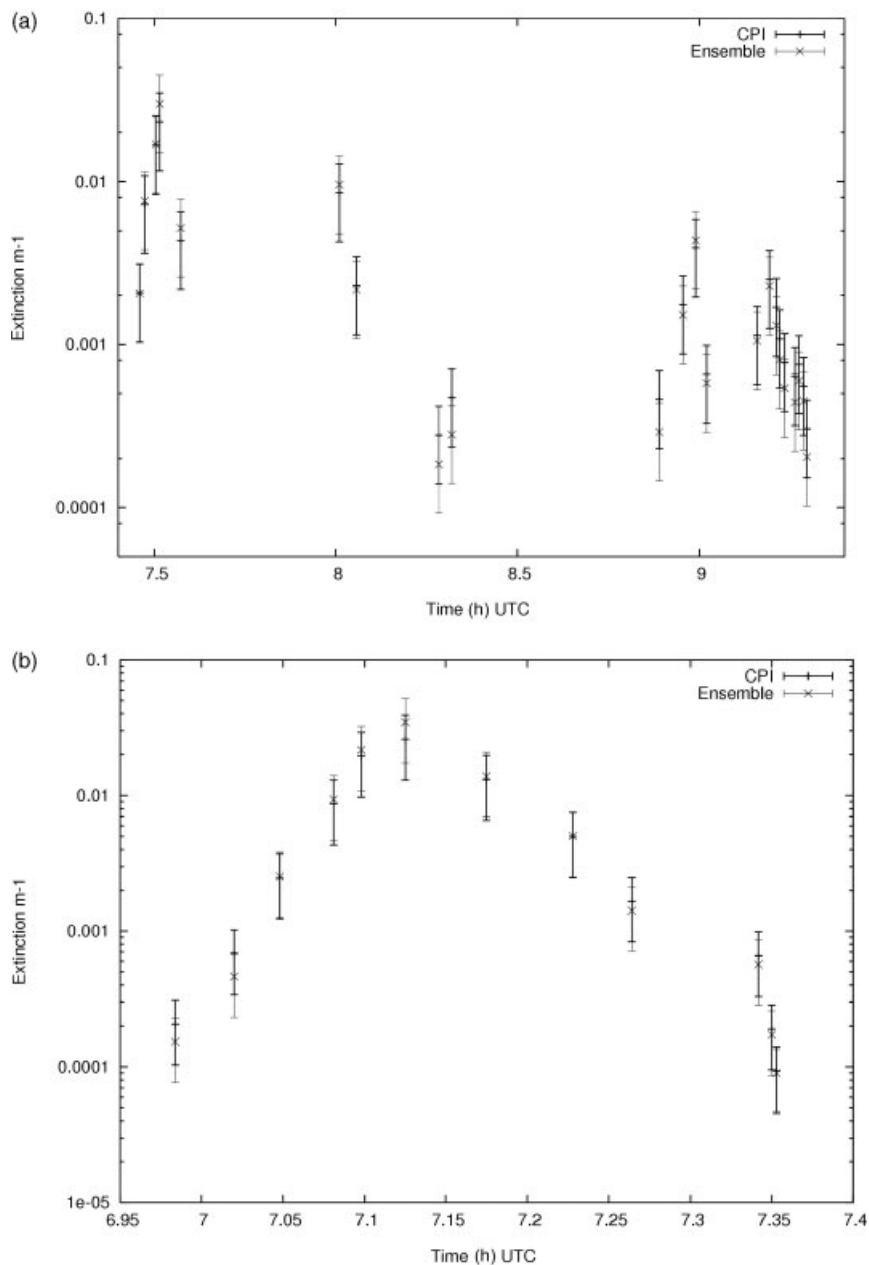
Figure 11. The CPI-estimated and ensemble model prediction of the volume extinction coefficient plotted as a function of time (UTC) with the experimental uncertainty of the CPI estimate shown as the bold error bar (CPI) and the ensemble model uncertainty is shown as the grey error bar (Ensemble).

that for cases AE10 and AE21 the uncertainty in the ensemble model prediction of the total solar optical depth is within the experimental uncertainty of the CPI estimates. The physical reasons for the ensemble model failing to predict the total solar optical depths for $\tau < 1$ are now explored in the next sub-sections in terms of the PSD.

4.3. The PSD

In order to physically understand as to why the ensemble model fails for $\tau < 1$, the *in situ* measured and parametrized PSDs are further explored in this sub-section using the case AE06 for the profile ascent shown in Figure 12(a), which had the lowest *in situ* estimated optical depth given in Table V. Similar to Figure 2, the *in situ* measured (averaged over the profile ascent) and parametrized PSDs are compared in Figure 13 for the case AE06. The figure shows that

the CPI for $l \leqslant 50\,\mu$m measures significantly fewer ice crystals than the CIP instrument, but for $l \geqslant 50\,\mu$m both instruments are generally within a factor 2 of each other. Also shown in the figure is the Field *et al.* (2007) tropical parametrization estimated using the CPI- and CIP-derived IWCs shown as the thin and bold full lines, respectively. In the case of the CPI-estimated IWC, the parametrized PSD is well below the *in situ* measured PSDs for $l \geqslant 50\,\mu$m; this underprediction of the PSD could account for the ensemble model predicted volume extinction being outside the range of the CPI uncertainty shown in Figure 12(a). In contrast, the uncertainty in the tropical parametrization using the CIP-estimated IWC is generally within the measured CIP PSD for $l \geqslant 60\,\mu$m. This difference between the CPI and CIP PSDs might also account for why the IWC PDFs for case AE06 only marginally passed the Mann–Whitney U test described in section 2.2.
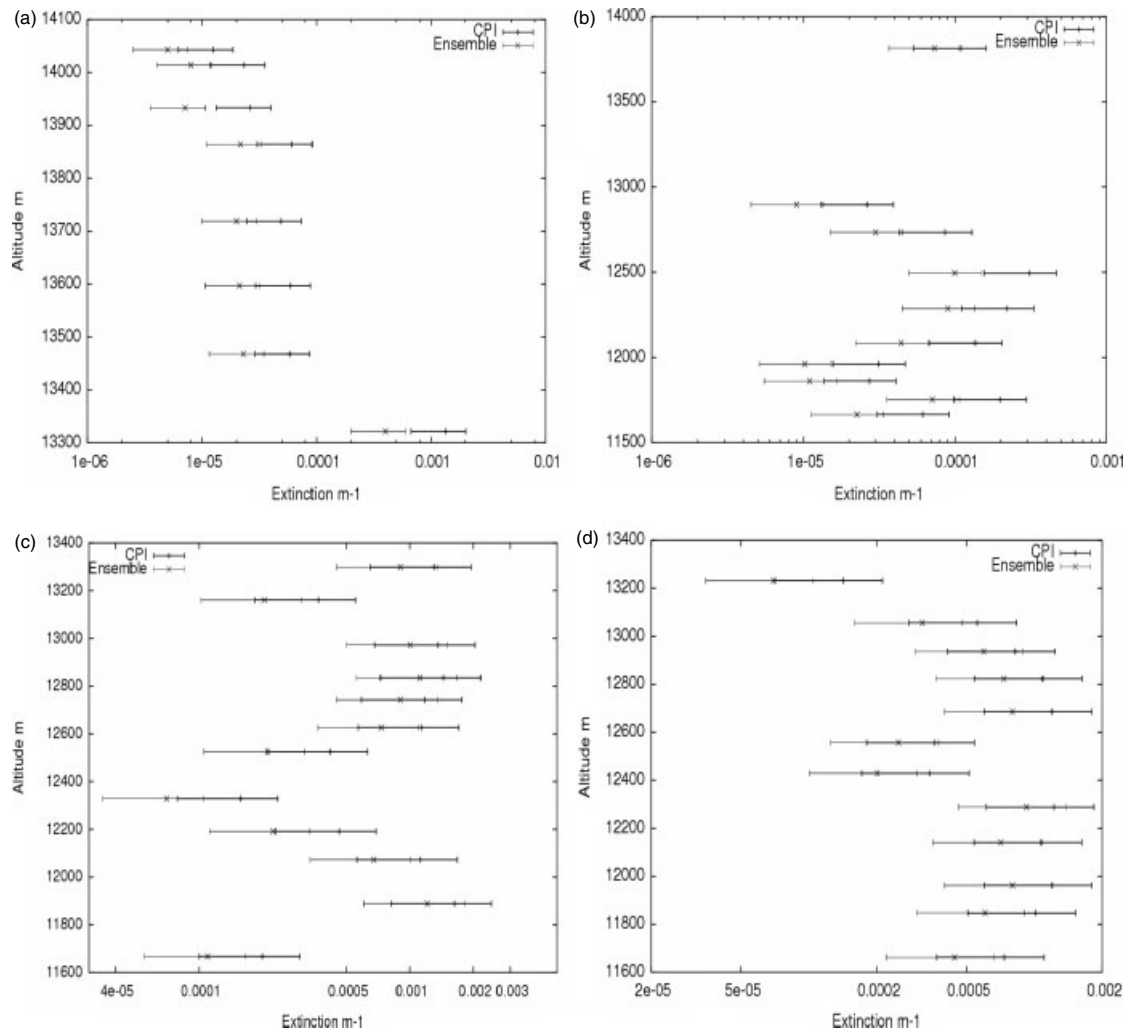
Figure 12. The CPI estimate and ensemble model prediction of the volume extinction coefficient as a function of altitude for the cases (a) AE06 (b) AE08 (c) AE10 and (d) AE21. The experimental uncertainty in the CPI estimate is shown as the bold error bar (CPI), and the ensemble model uncertainty is shown as the grey error bar (Ensemble).

Table V. Comparison of ensemble model prediction of the total solar optical depth with the CPI-estimated total solar optical depth for the integrated vertical profiles of volume extinction coefficient shown in Figure 12(a)–(d).

CASE	CPI	Ensemble
AE06	0.098 ± 0.05	0.03 ± 0.015
AE08	0.70 ± 0.35	0.20 ± 0.1
AE10	1.46 ± 0.73	1.013 ± 0.51
AE21	1.32 ± 0.66	0.862 ± 0.43

Given these differences between the two probes for this particular profile, the ensemble model-predicted extinction is recalculated, but using the CIP IWC to estimate the tropical and midlatitude parametrized PSDs. The tropical and midlatitude parametrized PSDs are then applied to the ensemble model. The results of this recalculation are shown in Figure 14. The figure shows that the uncertainty in the ensemble model-predicted extinction in now generally well within the CPI-estimated uncertainty for altitudes between about 13.5 and 13.7 km. For altitudes between about 13.9 and 14.1 km, the uncertainty in the ensemble model-predicted uncertainty tends to be toward the lower end of the CPI

uncertainty, though this is an improvement relative to Figure 12(a), where all ensemble model-predicted points were outside the CPI uncertainty for all altitudes. It should also be noted from Figure 14 that there is not a significant difference in the ensemble model-predicted extinction if either the tropical or midlatitude PSD parametrization is used. From the profile shown in Figure 14 using the tropical parametrization of the PSD, the ensemble model-predicted total optical depth is found to be 0.107 ± 0.05, which compares to the CPI estimated optical depth of 0.098 ± 0.05 from Table V. The ensemble model, assuming the CIP estimate of IWC to generate the tropical parametrized PSD to predict the total optical depth, is now well within the CPI uncertainty.

5. Summary

In this article the predictive value of a generalized ensemble model of cirrus ice crystals combined with a PSD scheme has been further investigated using tropical *in situ* macrophysical and microphysical data obtained from five cirrus cases during the ACTIVE campaign. The following *in situ* results were found:
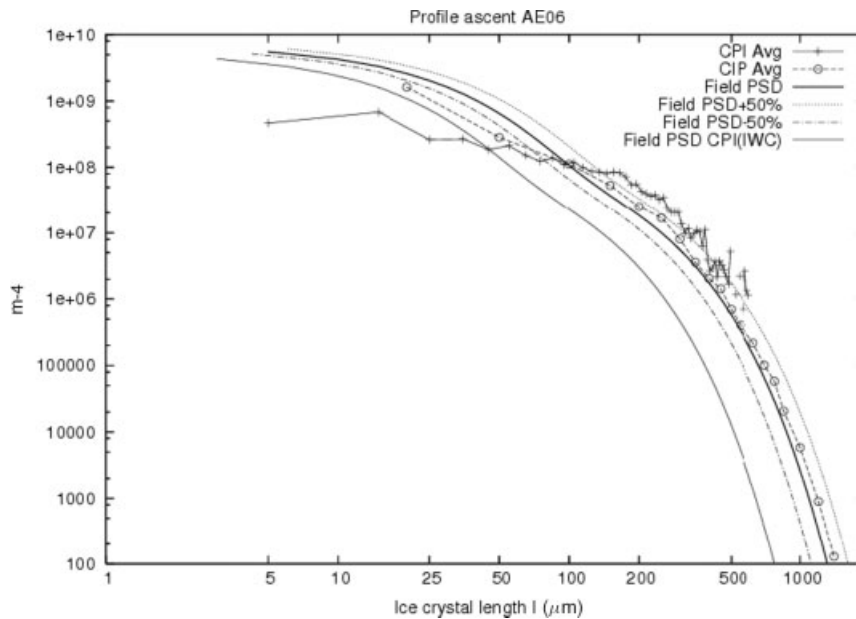
Figure 13. A comparison between the averaged CPI, CIP and Field *et al.* (2007) parametrizations of the ice crystal number density (m^{-4}) plotted against ice crystal length, l (μm) for the profile ascent obtained during AE06. The CPI and CIP measurements are represented by the full lines with crosses and dashed lines with open circles, respectively. The Field *et al.* (2007) parametrizations are represented by the bold solid line (CIP IWC) and thin solid line (CPI IWC), respectively. The +50% (Field PSD+50%) and −50% (Field PSD-50%) uncertainty in the CIP estimated tropical parametrization is represented by the dashed and dashed-dotted lines, respectively.

- Whilst noting the limitations of the CPIView-derived habit distributions, it was found that 80% or more of the shape distribution consisted of 'quasi-spherical' and small irregular ice crystals, with about 10% of the ice crystal population consisting of big irregulars. However, less than about 5% of the population was found to consist of single hexagonal columns or single hexagonal plates.
- From the vertical profiles, the CPI *in situ* estimates of the IWP ranged from about 1 ± 0.50 to $34 \pm 17 \, \text{g m}^{-2}$ and the total solar optical depth was estimated to be between about 0.1 ± 0.05 and 1.5 ± 0.75. From the straight and level runs, the maximum and minimum CPI IWC were estimated to be about 1 ± 0.50 and $0.003 \pm 0.0015 \, \text{g m}^{-3}$, respectively.

From the CPI-estimated IWC and in-cloud temperature, the PSD was estimated using the parametrization due to Field *et al.* (2007) and applied to the ensemble model effective density–size relationship to predict IWC and IWP. The same PSD parametrization was also applied to the ensemble model to predict the volume extinction coefficient and the total solar optical depth. The following results were obtained.

- In general, it was found that the ensemble model effective density–size relationship predicted uncertainties in the IWC and IWP which were within the uncertainties of the CPI estimates. However, the upper range of the ensemble model uncertainties tended to lie within the lower range of the CPI uncertainties as a function of altitude for cases AE06 and AE08.

In the case of the volume extinction coefficient and the total solar optical depth, τ, the predictive value of the ensemble model combined with the PSD scheme was found to be as follows.

- In terms of the volume extinction coefficient, it was found that, when the ensemble model was combined with the PSD scheme, the uncertainty in the prediction overlapped well with the CPI uncertainty for the straight and level runs conducted for cases AE04 and AE08 in regions of high to moderate IWC for all times considered.
- The uncertainty in the ensemble model prediction of the volume extinction coefficient as a function of altitude was shown to be generally within the experimental uncertainty of the CPI estimates when $\tau > 1$, though the upper range of the ensemble model uncertainty tended to be at the lower end of the CPI uncertainty.
- For cases where $\tau << 1$, the uncertainty in the ensemble model prediction of the volume extinction coefficient did not generally overlap with the experimental uncertainty of the CPI estimates.
- Similarly, when the total solar optical depth of the CPI estimates of $\tau > 1$, the ensemble model combined with the PSD scheme predicted an uncertainty in τ that was well within the experimental uncertainty of the CPI estimate.
- For the tropical cirrus cases where $\tau << 1$, the ensemble model combined with the PSD scheme did not predict an uncertainty in τ that was within the experimental uncertainty of the CPI estimates. For case AE06, the predicted τ was found to be 0.03 ± 0.015 compared to the CPI estimate of 0.098 ± 0.050.

In order to physically understand why the uncertainties in the ensemble model prediction of the volume extinction coefficient or total solar optical depth were not within the CPI uncertainties for $\tau << 1$, the PSD was further investigated. For case AE06, it was found that the CPI measured far fewer ice crystals for $l < 100 \, \mu$m and less ice mass for $l > 500 \, \mu$m than CIP, and as a consequence the
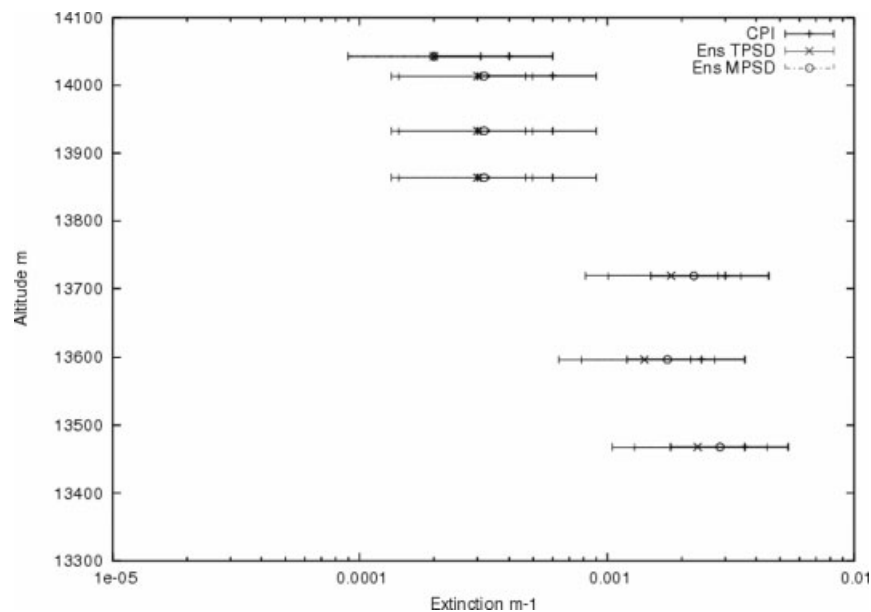
Figure 14. The CPI estimate and ensemble model prediction of the volume extinction coefficient (m^{-1}) as a function of altitude for the profile ascent obtained during AE06. The experimental uncertainty in the CPI estimate is shown as the bold error bar (CPI). The ensemble model uncertainty is shown as the grey error bar with the crosses using the tropical PSD parametrization (Ens TPSD), generated using the CIP IWC estimates. The ensemble model prediction using the midlatitude PSD parametrization (Ens MPSD) is shown as the dashed error bar with open circles.

CPI-estimated IWC could be underestimated. The reason for the CPI undercounting the small ice crystals might be the small sample volume. However, on using the CIP-estimated IWC to generate the parametrized PSDs, the uncertainties in the ensemble model-predicted volume extinction coefficient and total solar optical depth came within the CPI-estimated uncertainties.

In the tropical cirrus cases where $\tau << 1$, there are significant uncertainties remaining such as the lack of information on the shape of the PSD for in-cloud temperatures lower than $-60°C$ and low IWCs, ice crystal shape information for maximum dimensions less than about 100 μm and the role of ice crystal shattering on the inlet of *in situ* probes at such low in-cloud temperatures. If a generalized parametrization of the PSD is to be applied to ice crystal optical models, then the above measurements are sorely needed, since this cloud type is now known to be ubiquitous in the Tropics. Only if such information is obtained can the uncertainty in GCM prediction of climate change under CO_2 forcing be further reduced.

References

Baran AJ. 2009. A review of the light scattering properties of cirrus. *J. Quant. Spectrosc. Rad. Transf.* **110**: 1239–1260.

Baran AJ, Francis PN. 2004. On the radiative properties of cirrus cloud at solar and thermal wavelengths: A test of model consistency using high-resolution airborne radiance measurements. *Q. J. R. Meteorol. Soc.* **130**: 763–778.

Baran AJ, Labonnote LC. 2007. A self-consistent scattering model for cirrus. I: The solar region. *Q. J. R. Meteorol. Soc.* **133**: 1899–1912.

Baran AJ, Francis PN, Labonnote LC, Doutriaux-Boucher M. 2001. A scattering phase function for ice cloud: Tests of applicability using aircraft and satellite multi-angle multiwavelength radiance measurements of cirrus. *Q. J. R. Meteorol. Soc.* **127**: 2395–2416.

Baran AJ, Havemann S, Francis PN, Watts PD. 2003. A consistent set of single-scattering properties for cirrus cloud: Tests using radiance measurements from a dual-viewing multi-wavelength satellite-based instrument. *J. Quant. Spectrosc. Rad. Transf.* **79–80**: 549–567.

Baran AJ, Connolly PJ, Lee C. 2009. Testing an ensemble model of cirrus ice crystals using mid-latitude *in situ* estimates of ice water content, volume extinction coefficient, and the total solar optical depth. *J. Quant. Spectrosc. Rad. Transf.* **110**: 1579–1598.

Baum BA, Heymsfield AJ, Yang P, Bedka ST. 2005. Bulk scattering properties for the remote sensing of ice clouds. Part I. Microphysical data and models. *J. Appl. Meteorol.* **44**: 1885–1895.

Baum BA, Yang P, Nasiri S, Heidinger AK, Heymsfield A, Li J. 2007. Bulk scattering properties for the remote sensing of ice clouds. Part III: High-resolution spectral models from 100 to 3250 cm^{-1}. *J. Appl. Meteorol.* **46**: 423–434.

Brown PRA, Francis PN. 1995. Improved measurements of the ice water content in cirrus using an evaporative technique. *J. Atmos. Oceanic Technol.* **12**: 410–414.

Choi Y-S, Ho C-H. 2006. Radiative effects of cirrus with different optical properties over the tropics in MODIS and CERES observations. *Geophys. Res. Lett.* **33**: L21811.

Connolly PJ, Saunders CRP, Gallagher M, Bower KN, Flynn MJ, Choularton TW, Whiteway J, Lawson RP. 2005. Aircraft observations of the influence of electric fields on the aggregation of ice crystals. *Q. J. R. Meteorol. Soc.* **131**: 1695–1712.

Connolly PJ, Flynn MJ, Ulanowski Z, Choularton TW, Gallagher MW, Bower KN. 2007. Calibration of the cloud particle imager probes using calibration beads and ice crystal analogs: The depth of field. *J. Atmos. Oceanic Technol.* **24**: 1860–1879.

Donner L, Seman CJ, Soden BJ, Hemler RS, Warren JC, Strom J, Liou KN. 1997. Large-scale ice clouds in the GFDL SKYHI general circulation model. *J. Geophys Res.* **102**: 21745–21768.

Edwards JM, Havemann S, Thelen J-C, Baran AJ. 2007. A new parametrization for the radiative properties of ice crystals: Comparison with existing schemes and impact in a GCM. *Atmos. Res.* **83**: 19–35.

Field PR, Wood R, Brown PR, Kaye PH, Hirst E, Greenway R, Smith JA. 2003. *J. Atmos. Oceanic Technol.* **20**: 249–261.

Field PR, Hogan RJ, Brown PRA, Illingworth AJ, Choularton TW, Cotton RJ. 2005. Parametrization of ice-particle size distribution functions for midlatitude stratiform cloud. *Q. J. R. Meteorol. Soc.* **131**: 1997–2017.

Field PR, Heymsfield AJ, Bansemer A. 2006. Shattering and particle interarrival times measured by optical array probes in ice clouds. *J. Atmos. Oceanic Technol.* **23**: 1357–1371.

Field PR, Heymsfield AJ, Bansemer A. 2007. Snow size distribution parameterization for mid-latitude and tropical ice cloud. *J. Atmos. Sci.* **64**: 4346–4365.

Francis PN, Foot JS, Baran AJ. 1999. Aircraft measurements of the solar and infrared radiative properties of cirrus and their dependence on ice crystal shape. *J. Geophys. Res.* **104**: 31685–31695.

Fu Q. 2007. A new parameterization of an asymmetry factor of cirrus clouds for climate models. *J. Atmos. Sci.* **64**: 4140–4150.

Heymsfield AJ. 2007. On measurements of small ice particles in clouds. *Geophys. Res. Lett.* **34**: L23812.

Heymsfield AJ, Lewis S, Bansemer A, Iaquinta J, Miloshevich LM, Kajikawa M, Twohy C, Poellot MR. 2002. A general approach for deriving the properties of cirrus and stratiform ice cloud particles. *J. Atmos. Sci.* **59**: 3–29.

Heymsfield AJ, Bansemer A, Schmitt C, Twohy C, Poellot M. 2004. Effective ice particle densities derived from aircraft data. *J. Atmos. Sci.* **61**: 982–1003.

Hong G, Yang P, Gao BC, Baum BA, Hu YX, King MD, and Platnick S. 2007. High cloud properties from three years of MODIS Terra and Aqua collection-4 data over the tropics. *J. Appl. Meteorol. Climatol.* **46**: 1840–1856.

IPCC. 2007. *Contribution of Working Group I to the Fourth Assessment Report of the Intergovernmental Panel on Climate Change. 2007.* Solomon S, Qin D, Manning M, Chen Z, Marquis M, Averyt KB, Tignor M, Miller HL. (eds.) Cambridge University Press: Cambridge, UK.

Jensen EJ, Pfister L, Bui TV, Lawson P, Baker B, Mo Q, Baumgardner D, Weinstock EM, Smith JB, Moyer EJ, Hanisco TF, Sayres DS, St Clair JM, Alexander MJ, Toon OB, Smith JA. 2008. Formation of large (similar or equal to 100 μm) ice crystals near the tropical tropopause. *J. Atmos. Chem. Phys.* **8**: 1621–1633.

Jourdan O, Oshchepkov S, Shcherbakov V, Gayet JF, Isaka H. 2003. Assessment of cloud optical parameters in the solar region: Retrievals from airborne measurements of scattering phase functions. *J. Geophys. Res.* **108**: 4572.

Kristjánsson JE, Edwards JM, Mitchell DL. 2000. The impact of a new scheme for the optical properties of ice crystals on the climate of two GCMs. *J. Geophys. Res.* **105**: 10063–10079.

Lawson RP, Baker BA, Schmitt CG, Jensen TL. 2001. An overview of microphysical properties of Arctic clouds observed in May and July during FIRE.ACE. *J. Geophys. Res.* **106**: 14989–15014.

Lawson RP, Baker BA, Pilson BL. 2003. '*In situ* measurements of microphysical properties of mid-latitude and anvil cirrus and validation of satellite retrievals'. Paper no. TS 32.4 in *Proceedings of the 30th International Symposium on Remote Sensing of Environment*, Honolulu, Hawaii.

Lawson RP, Pilson B, Baker B, Mo Q, Jensen E, Pfister L, Bui P. 2008. Aircraft measurements of microphysical properties of subvisual cirrus in the tropical tropopause layer. *Atmos. Chem. Phys.* **8**: 1609–1620.

Liou KN. 1986. Influence of cirrus clouds on weather and climate processes: A global perspective. *Mon. Weather. Rev.* **114**: 1167–1199.

Liou KN, Takano Y, Yang P. 2000. Light scattering and radiative transfer by ice crystal clouds: Applications to climate research. In *Light scattering by nonspherical particles: Theory, measurements, and geophysical applications.* Mishchenko MI, Hovenier JW, Travis LD. (eds.) Academic Press: San Diego, California. 417–449.

Lynch DK, Sassen K, Star D, Stephens GL. 2002. *Cirrus.* Oxford University Press: Oxford, UK.

Matrosov SY. 1999. Retrievals of vertical profiles of ice cloud microphysics from radar and IR measurements using tuned regressions between reflectivity and cloud parameters. *J. Geophys. Res.* **104**: 16741–16753.

May PT, Mather JH, Vaughan G, Jakob C, McFarquhar GM, Bower K, Mace GG. 2009. Aerosol and thermodynamic effects on tropical cloud systems during TWPICE and ACTIVE. *Atmos. Chem. Phys.* **9**: 15–24.

McFarquhar GM, Heymsfield AJ. 1996. Microphysical characteristics of three anvils sampled during the central equatorial Pacific experiment. *J. Atmos. Sci.* **53**: 2401–2423.

McFarquhar GM, Yang P, Macke A, Baran AJ. 2002. A new parameterization of single scattering solar radiative properties for tropical anvils using observed ice crystal size and shape distributions. *J. Atmos. Sci.* **59**: 2458–2478.

McFarquhar GM, Um J, Freer M, Baumgardner D, Kok GL, Mace G. 2007. Importance of small ice crystals to cirrus properties: Observations from the Tropical Warm Pool International Cloud Experiment (TWP-ICE). *Geophys. Res. Lett.* **34**: L13803.

Platnick S, King MD, Ackerman SA, Menzel WP, Baum BA, Riedi JC, Frey RA. 2003. The MODIS cloud products: Algorithms and examples from Terra. *IEEE. Trans. Gesosci. Remote Sens.* **41**: 459–473.

Rolland P, Liou KN, King MD, Tsay SC, McFarquhar GM. 2000. Remote sensing of optical and microphysical properties of cirrus clouds using MODIS channels: Methodology and sensitivity to assumptions. *J. Geophys. Res.* **105**: 11721–11738.

Sassen K, Comstock JM. 2001. A mid-latitude cirrus cloud climatology from the facility for atmospheric remote sensing. Part III: Radiative properties. *J. Atmos. Sci.* **58**: 2113–2127.

Sassen K, Wang Z, Liu D. 2008. Global distribution of cirrus clouds from CloudSat/Cloud-Aerosol lidar and infrared pathfinder satellite observations (CALIPSO) measurements. *J. Geophys. Res.* **113**: D00A12.

Stephens GL, Tsay S-C, Stackhouse PW, Flatau PJ. 1990. The relevance of the microphysical and radiative properties of cirrus clouds to climate and climatic feedback. *J. Atmos. Sci.* **47**: 1742–1753.

Stith JL, Dye J, Heymsfield AJ, Grainger CA. 2000. 'Microphysical features in tropical clouds'. In *Proceedings of the 13th international conference on clouds and precipitation*, 14–18 August 2000, Reno, Nevada, USA. 1245–1248.

Stoelinga MT, Locatelli JD, Woods CP. 2007. The occurrence of 'irregular' ice particles in stratiform clouds. *J. Atmos. Sci.* **64**: 2740–2750.

Stubenrauch CJ, Chédin A, Rädel G, Scott NA, Serrar S. 2006. Cloud properties and their seasonal and diurnal variability from TOVS Path-B. *J. Climate* **19**: 5531–5553.

Um J, McFarquhar G. 2009. Single scattering properties of aggregates of plates. *Q. J. R. Meteorol. Soc.* **135**: 291–304.

van de Hulst HC. 1957. *Light Scattering by Small Particles.* J. Wiley & Sons: New York.

Vaughan G, Schiller C, Mackenzie AR, Bower K, Peter T, Schlager H, Harris NRP, May PT. 2008. Studies in a natural laboratory: High-altitude aircraft measurements around deep tropical convection. *Bull. Amer. Meteorol. Soc.* **89**: 647–662.

Waliser DE, Li JLF, Woods CP, Austin RT, Bacmeister J, Chern J, Del Genio A, Jiang JH, Kuang ZM, Meng H, Minnis P, Platnick S, Rossow WB, Stephens GL, Sun-Mack S, Tao WK, Tompkins AM, Vane DG, Walker C, Wu D. 2009. Cloud ice: A climate model challenge with signs and expectations of progress. *J. Geophys. Res.* **114**: D00A21.

Whiteway J, Cook C, Gallagher M, Chourlarton T, Harries J, Connolly P, Busen R, Bower K, Flynn M, May P, Aspey R, Hacker J. 2004. Anatomy of cirrus clouds: Results from the Emerald airborne campaigns. *Geophys. Res. Lett.* **31**: L24102, DOI:10.1029/2004GL021201.

Wilson DR, Ballard SP. 1999. A microphysically based precipitation scheme for the UK Meteorological Office Unified Model. *Q.J.R. Meteorol. Soc.* **125**: 1607–1636.

Wylie DP, Menzel WP. 1999. Eight years of high cloud statistics using HIRS. *J. Climate.* **12**: 170–184.

Yang P, Baum BA, Heymsfield AJ, Hu YX, Huang HL, Tsay SC, Ackerman S. 2003. Single-scattering properties of droxtals. *J. Quant. Spectrosc. Rad. Transf.* **79–80**: 1159–1180.

Zhang Y, Macke A, Albers F. 1999. Effect of crystal size spectrum and crystal shape on stratiform cirrus radiative forcing. *Atmos. Res.* **52**: 59–75.